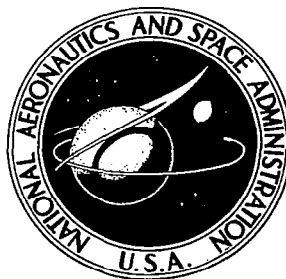


**NASA CONTRACTOR
REPORT**

NASA CR-950



NASA CR

0060025



TECH LIBRARY KAFB, NM

**IMPLOSIVELY ACCELERATED
SHOCK TUBE DRIVER**

by Stephen P. Gill and Robert C. Goettelman

Prepared by

STANFORD RESEARCH INSTITUTE

Menlo Park, Calif.

for Ames Research Center



NATIONAL AERONAUTICS AND SPACE ADMINISTRATION • WASHINGTON, D. C. • NOVEMBER 1967

IMPLOSIVELY ACCELERATED SHOCK TUBE DRIVER

By Stephen P. Gill and Robert C. Goettelman

Distribution of this report is provided in the interest of information exchange. Responsibility for the contents resides in the author or organization that prepared it.

Issued by Originator as SRI Project FGU-5694

Prepared under Contract No. NAS 2-3129 by
STANFORD RESEARCH INSTITUTE
Menlo Park, Calif.

for Ames Research Center

NATIONAL AERONAUTICS AND SPACE ADMINISTRATION

ABSTRACT

The feasibility of using an implosive driver in a shock tube facility for research in high energy gasdynamics was investigated. Two implosive shock tube systems, one using a jetting driver and the other a jetless driver, were used to drive shock waves at velocities from 11 to 15 km/sec into dry air at initial pressures in the range 0.5 to 5 torr. The characteristics of the driver were investigated in a combined experimental and theoretical program, and the high energy gas flow behind the shock front was studied to determine experimentally its uniformity, purity, duration, and quality.

It is concluded that the jetting driver, which consists of a cylinder of high explosive that progressively collapses a glass tube and projects a diffuse glass jet into the shock tube, can be of significant value as a shock tube driver for initial test gas pressures less than 1 torr. The diffuse glass jet is as effective as a perfect piston at these pressures, and a plane shock of nearly uniform velocity is driven into the test gas, followed by high energy flow of exceptional uniformity, quality, and purity. In addition, the test time grows at a rate nearly equal to that calculated for a perfect piston, and is insensitive to boundary layer phenomena.

A quantitative theory has been developed which describes the operation of the jetting driver, the detailed properties of the driving jet, and the growth of test time in the shock tube. The existing data correlate well on the basis of this theory, but additional data must be collected to provide a definitive comparison between theory and experiment.

The jetless driver, which is used in a manner closely resembling a conventional shock tube, was only briefly studied because difficulties with interface mixing and boundary layer limitation of test time were foreseen. The experimental results directly confirm the predictions of a well known boundary layer theory of test time growth, and indicate a

minimal amount of interface mixing. The usefulness of this jetless driver system is severely reduced at low test gas pressures because of the boundary layer phenomenon, and at pressures below 1 torr the jetting driver is superior.

CONTENTS

ABSTRACT	iii
LIST OF ILLUSTRATIONS.	vii
LIST OF TABLES	ix
1. INTRODUCTION	1
2. INSTRUMENTATION.	3
2.1 Experimental Facilities	3
2.2 Experimental Techniques	4
2.2.1 Backlighting	4
2.2.2 Emissivity and Temperature Measurements.	4
2.3 Conductivity Gage	9
3. EXPERIMENTAL RESULTS	15
3.1 Jetting Driver.	15
3.1.1 Driver Characteristics	15
3.1.2 Test Gas Flow Properties	22
3.2 Jetless Driver.	36
4. THEORETICAL CALCULATIONS	39
4.1 Properties of High Temperature Air.	39
4.1.1 Thermodynamic Properties	39
4.1.2 Shock Calculations	42
4.1.3 Radiative Properties	43
4.2 Boundary Layer Effects.	44
4.2.1 Two-Gas System	44
4.2.2 One-Gas System	46
4.3 Radiative Cooling	47
4.4 Conductivity Gage Analysis.	49
4.4.1 DC Conductivity Gage	49
4.4.2 RF Gage.	54
5. CONCLUSIONS.	57
5.1 Jetting Driver.	57
5.2 Jetless Driver.	57
5.3 Measurement Techniques.	58
6. RECOMMENDATIONS FOR FUTURE WORK.	59
6.1 Laboratory Containment.	59
6.2 Gas Properties.	59
6.3 Simulation Studies.	59
REFERENCES	61

ILLUSTRATIONS

Fig. 1. 1	An Implosive Driver	1
Fig. 2. 1	Spectral Response of Film	7
Fig. 2. 2	Film Calibration Curve for Temperature Measurements	8
Fig. 2. 3	Conductivity Gage A	11
Fig. 2. 4	Conductivity Gage B	12
Fig. 3. 1	Implosive Driver Configurations	16
Fig. 3. 2	Flash X-Ray of the Implosive Collapse Region	17
Fig. 3. 3	Glass Jet Impacting an Illuminated End Plate	20
Fig. 3. 4	Streak Camera Record of Shot 12,124	21
Fig. 3. 5	Streak Camera Record of Shot 12,123	23
Fig. 3. 6	Shock Velocity <i>vs.</i> Travel Distance for the Jetting Driver	24
Fig. 3. 7	Test Time <i>vs.</i> Shock Travel Distance for the Nitromethane Jetting Driver	25
Fig. 3. 8	Test Time <i>vs.</i> Shock Travel Distance for the C2 Jetting Driver	27
Fig. 3. 9	Mass Flux Through the Diffuse Piston as a Function of Initial Air Pressure	29
Fig. 3.10	Flow Around Conductivity Gage A	30
Fig. 3.11	Flow Around Conductivity Gage B	31
Fig. 3.12	RF Conductivity Gage Records	32
Fig. 3.13	Time-Resolved Spectrograph of Shot 12,438	33
Fig. 3.14	Time-Resolved Spectrograph of Shot 12,472	34
Fig. 3.15	Test Time <i>vs.</i> Shock Travel Distance for the Jetless Driver	37
Fig. 3.16	Time-Resolved Spectrograph of Shot 12,481	38
Fig. 4. 1	The Thermodynamic and Radiative Properties of High Temperature Air	41
Fig. 4. 2	Radiative Cooling Curve for Air	48
Fig. 4. 3	DC Conductivity Gage Integral	52

TABLES

Table 3.1	Shot Record	18
Table 3.2	Theoretical Values of Driver Jet Mass	19
Table 3.3	Experimentally Determined Emissivity and Temperature.	35

1. INTRODUCTION

This project was initiated to determine the feasibility of using an implosive driver system to generate an environment suitable for experimental research in high temperature gasdynamics and the aerophysics of re-entry at satellite velocities.

Under a previous contract with NASA (Contract No. NAS2-1361), an implosive driver was developed to provide a high pressure reservoir of light gas for accelerating hypervelocity projectiles. In the work on that contract several configurations were tested, evaluated, and optimized for use as high pressure drivers. One such system which was successfully employed (see Fig. 1.1) consists of a cylindrical charge of nitromethane or Composition C3 explosive concentric about a glass tube. Detonation of the explosive leads to progressive collapse of the tube and the formation of a diffuse jet which drives a plane shock into the driver gas. A complete description of this system and the experimental results obtained in driving high pressure helium (1 to 20 atm initial pressure) may be found in the contractual reports.^{1,2}

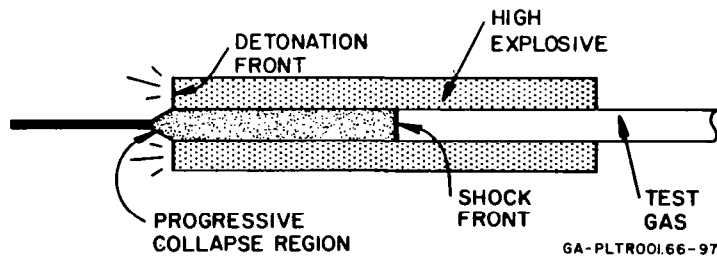


FIG. 1.1 AN IMPLOSIVE DRIVER

It was clear at the beginning of the present program that the implosive driver system offers a much greater range of energy capabilities than does a conventional shock tube. However, information was lacking concerning the duration, quality, uniformity, and purity of the high energy test gas behind the shock front. It was therefore decided that a major goal of the project would be to develop instrumentation suitable for

making detailed measurements on the operation of the driver system and on the properties of the resultant high energy gas flow, and to use this instrumentation to determine whether the flow has characteristics suitable for research in high energy gasdynamics.

The experimental program has essentially followed the original concept. Two different shock tube systems, one based on the jetting and one on the jetless driver, have been tested with streak and framing photography, time-resolved spectroscopy, and specially designed instrumentation. The results indicate that both types of driver produce clean, uniform flow with a test time dependent on initial pressure. The experimental apparatus used in making these measurements is described in Sec. 2 and the experimental results are detailed in Sec. 3.

2. INSTRUMENTATION

2.1 Experimental Facilities

Much of the experimental data collected for this research project was obtained at an explosives test site operated by Poulter Laboratories and located approximately 30 miles from Menlo Park. This site is fully instrumented with the high speed photographic and electronic equipment necessary to make the microsecond-type measurements required in shock wave experiments. The more important facilities used in shock propagation studies are streak and framing cameras. Two streak cameras are available. The smaller is a 35 mm camera with a maximum writing speed of $3.84 \text{ mm}/\mu\text{sec}$. The larger is a Beckman and Whitley Model 770 that uses 70 mm film and has a maximum writing speed of $10 \text{ mm}/\mu\text{sec}$. These cameras are located in a bombproof building completely instrumented with the necessary supplemental electronic delays, counters, detonator units, and other equipment so that high precision recording of shock wave events may be easily performed. The Dynafax framing camera is capable of a total of 224 frames at a maximum rate of 35,000 frames/sec on 16 mm film. The Beckman and Whitley 189 framing camera is capable of 25 frames at a maximum rate of 2.6×10^6 frames/sec on 35 mm film. The Beckman and Whitley Model 501 single frame image converter camera (ICC) is capable of 5 nsec resolution. These framing cameras are supplemented with the necessary electronic timing equipment. A flash X-ray site is also available.

Poulter Laboratories and Beckman and Whitley, Inc., have jointly designed and constructed a time-resolving spectrograph now in use at the Calaveras Test Site.³ The spectrograph was designed to provide the maximum photographic aperture possible, commensurate with reasonable wavelength resolution and time resolution. The limiting aperture of all the optics used is $f/2.5$ and the grating used is of a highly efficient design with rulings blazed for maximum reflection into the first order visible spectrum. The maximum wavelength resolution achieved by this instrument is approximately 3\AA and the time resolution is approximately 50 nsec at maximum speed.

Film processing, except for color film, is performed at the Calaveras Test Site under closely controlled conditions. Film analysis equipment

maintained at the Menlo Park Laboratories includes a fully digitalized Benson-Lehner Telereadex film reader, Model 29E-39. The output of the Telereadex can be directly transcribed onto IBM cards for automatic data processing. A Baird scanning microdensitometer with a graphical recording unit is used for reducing data from the time-resolving spectrograph.

2.2 Experimental Techniques

2.2.1 Backlighting

An argon bomb light source was used as a calibrated standard for several temperature and emissivity measurements during the project. The argon bomb consists of a P-40 explosive plane wave generator and 1-in. pad of Comp B explosive; on detonation the explosive drives a strong shock wave into a 4-in.-diameter tube filled with argon gas at atmospheric pressure. The intense luminosity at the shock front, probably produced by ion-electron recombinations in the shocked argon, has been extensively studied for use in high speed photography.⁴

The radiation signature of the light source consists of a rise time of approximately 0.5 μ sec, a dwell time at maximum intensity of approximately 3 μ sec, and thereafter a steady decrease in intensity. Roth⁴ conjectures that the rise time is due to the finite thickness of shocked argon necessary to achieve blackbody radiation, and that the subsequent decrease in intensity is due to absorption of visible radiation by unshocked argon which has been heated by absorbing ultraviolet radiation from the shocked front.

Roth has measured the peak light intensity from the shock front in the wavelength interval 3600 - 6000 \AA using a calibrated photomultiplier and interference filter system, and has determined that the radiation is that of a black body at a temperature of $29,000 \pm 1000^\circ\text{K}$.

2.2.2 Emissivity and Temperature Measurements

Several different techniques for obtaining time-resolved emissivity and temperature measurements of the shocked test gas were used during this project. The accuracy of the measurements depends principally on photometric techniques for comparing relative light intensities, and on the accuracy of the calibration of the light source described above.

All measurements were made over a wavelength range corresponding to the spectral sensitivity of the film, and no effort was made to restrict this range by the use of optical filters. Because of the wide spectral range, short exposure times (on the order of 100 nsec) were feasible; a narrow wavelength interval would require longer exposure times and would degrade the time resolution of the data.

The simplest technique for determining the emissivity of the shocked test gas consists of placing a reflecting mirror behind a section of the glass shock tube and observing the flow with a streak camera or a framing camera. A comparison of the light intensities at a given position behind the shock front with and without the reflecting mirror is sufficient to determine the emissivity of the gas, and a comparison of the emitted intensity with a blackbody light source of known temperature is sufficient to determine the gas temperature once the emissivity is known.

Let ϵ be the emissivity of the gas at a wavelength λ and a position ξ behind the shock front; let I_1 be the measured radiance without a backing mirror; and let I_2 be the measured radiance with the mirror behind the gas. If we suppose the gas to be in local thermal equilibrium at a temperature T and denote the blackbody radiance at that temperature by $N_\lambda(T)$ we have:

$$I_1 = \epsilon N_\lambda(T) \quad (2.1)$$

$$I_2 = I_1 + (1 - \epsilon)I_1 \quad (2.2)$$

The emissivity may be determined directly from the ratio I_2/I_1 , as may be verified by reference to Eq. 2.2:

$$\epsilon = 2 - I_2/I_1 \quad (2.3)$$

By comparing I_1 to the intensity of a black body at a known reference temperature T_0 we may determine the temperature of the gas. Let the measured radiance of the light source be I_0 ; we then have

$$I_0 = N_\lambda(T_0) \quad (2.4)$$

and, from Eq. 2.1,

$$N_\lambda(T)/N_\lambda(T_0) = I_1/(\epsilon I_0) \quad (2.5)$$

Knowing the reference temperature T_0 we may determine T by referring to tables of the blackbody radiation function.

The equations described above are valid only at a definite wavelength; to find the equivalent equations valid over a range of wavelengths we use integral relations and define an average emissivity. Thus we have

$$\bar{I}_0 = \int A N_\lambda(T_0) d\lambda \quad (2.6)$$

$$\bar{I}_1 = \int \epsilon A N_\lambda(T) d\lambda \quad (2.7)$$

$$\bar{I}_2 = \bar{I}_1 + \int (1 - \epsilon) A N_\lambda(T) d\lambda \quad (2.8)$$

where $A(\lambda)$ is the relative spectral response of the film. The average emissivity is then defined by the equation

$$\bar{\epsilon} = 2 - \bar{I}_2/\bar{I}_1 \quad (2.9)$$

and the temperature is defined by the equation

$$\int A N_\lambda(T) d\lambda / \int A N_\lambda(T_0) d\lambda = \bar{I}_1 / (\bar{\epsilon} \bar{I}_0) \quad (2.10)$$

The equations for the average emissivity and temperature are exact if the emissivity is independent of wavelength, and are expected to provide a reasonable estimate if the emissivity is a slowly varying function of wavelength. The time-resolved spectrographic records of the radiation from the test gas do in fact show a continuous spectrum, so that average emissivity and temperature measurements are probably valid. Equation 2.10 may be solved for the gas temperature T by constructing a calibration curve. For every value of T the two integrals on the left-hand side of the equation are numerically integrated using the blackbody radiation function tables. This defines a function $R(T)$ which depends on the film sensitivity curve and the reference temperature and provides the desired relationship between the gas temperature T and the experimental value of $\bar{I}_1/(\bar{\epsilon} \bar{I}_0)$.

Typical spectral response curves are shown in Fig. 2.1. Calculations are greatly simplified if the spectral response curve is approximated by the idealized curve consisting of a constant response in the range

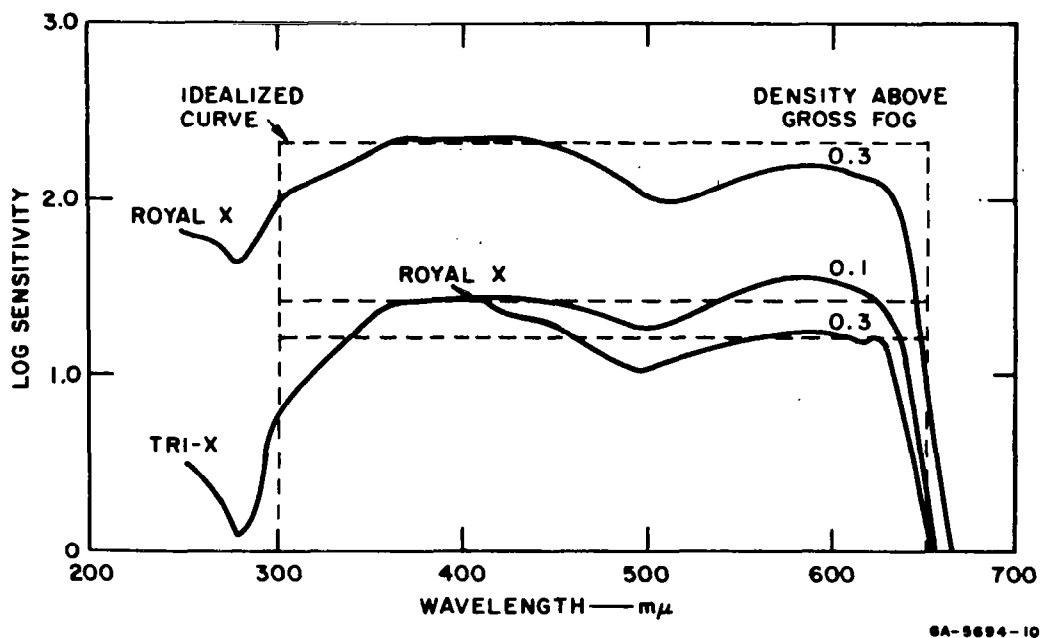


FIG. 2.1 SPECTRAL RESPONSE OF FILM

$\lambda_1 = 3000\text{\AA}$ to $\lambda_2 = 6500\text{\AA}$, and zero response outside this range. The function of temperature defined by Eq. 2.10,

$$R(T) = \frac{\int_{\lambda_1}^{\lambda_2} N_{\lambda}(T) d\lambda}{\int_{\lambda_1}^{\lambda_2} N_{\lambda}(T_0) d\lambda} \quad , \quad (2.11)$$

may then be obtained by referring to tables of the blackbody radiation functions; it is plotted in Fig. 2.2. This curve, together with an experimental determination of $\bar{I}_1/(\epsilon\bar{I}_0)$, suffices to determine the temperature of the gas.

Conversely, if the temperature of the gas is assumed to be the value calculated from the Hugoniot conservation equations coupled with the equilibrium thermodynamic properties of the gas, then the emissivity of the gas may be determined from the calibration curve and an experimental measurement of the ratio \bar{I}_1/\bar{I}_0 :

$$\bar{\epsilon} = \bar{I}_1/[\bar{I}_0 R(T)] \quad . \quad (2.12)$$

The emissivity determined in this manner depends upon only a single measurement, \bar{I}_1 , of the shocked gas radiation, which is the principal advantage of the method.

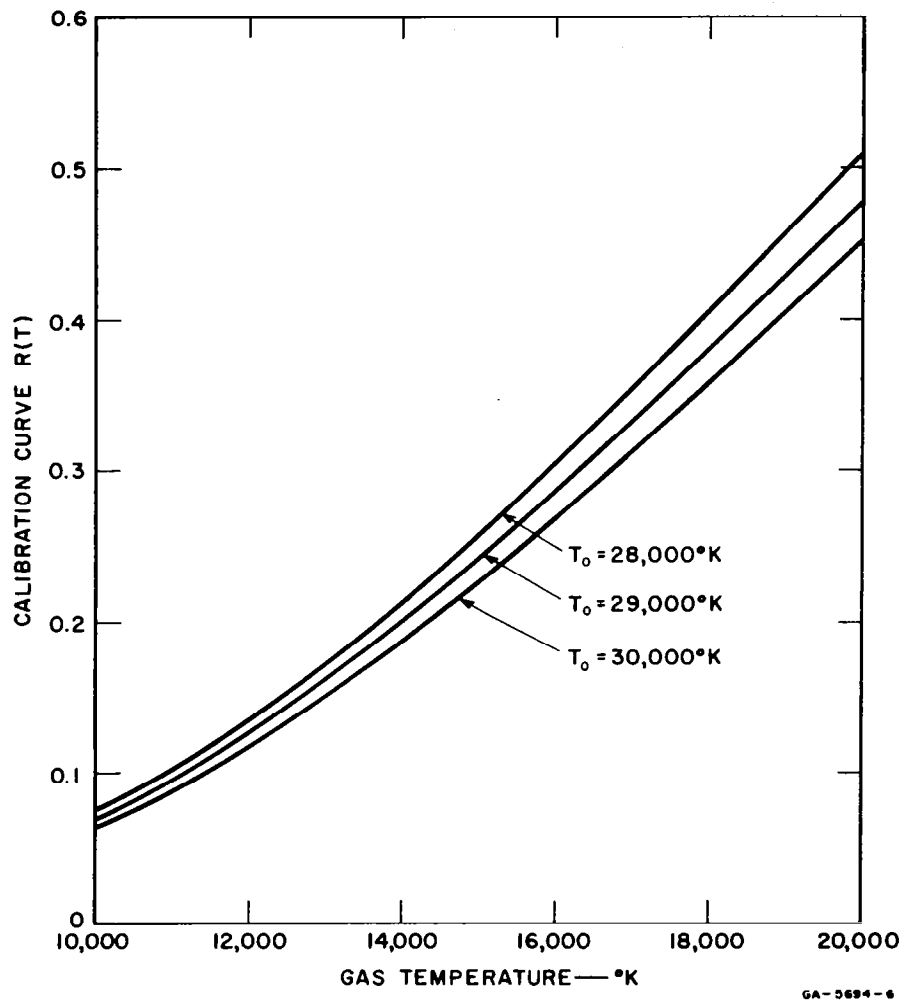


FIG. 2.2 FILM CALIBRATION CURVE FOR TEMPERATURE MEASUREMENTS

Another technique for determining the emissivity of the gas is to observe a backlight through the shocked gas. At a given wavelength the measured radiance of the backlight test gas would be given by

$$I_3 = I_1 + (1 - \epsilon)I_B \quad (2.13)$$

Here, as before, I_1 is the measured radiance of the test gas itself. I_B is the measured radiance of the backlight which, because of the decay in intensity of the argon light source, will generally be less than I_0 , the standard intensity reference.

By rearranging Eq. 2.13 it is apparent that the emissivity depends only upon the ratios of observed intensities:

$$\epsilon = 1 + I_1/I_B - I_3/I_B \quad (2.14)$$

These equations are of course valid only at a certain wavelength; for a finite wavelength interval they are replaced as before by an integral over the wavelength range:

$$\bar{I}_3 = \int \epsilon AN_\lambda(T) d\lambda + \int (1 - \epsilon) AN_\lambda(T_B) d\lambda \quad (2.15)$$

We then define an average emissivity based on the measured intensity ratios which is exact if the emissivity is independent of wavelength:

$$\bar{\epsilon} = 1 + \bar{I}_1/\bar{I}_B - \bar{I}_3/\bar{I}_B \quad (2.16)$$

The three different methods for determining emissivity—the reflecting mirror, backlighting, and assuming a temperature—were all used during the course of the project. Where it was possible to apply more than one method, the results agree with one another within the limits of experimental accuracy.

2.3 Conductivity Gage

During this project a gage was developed to measure the scalar conductivity of the ionized test gas. The original intent in designing the gage was to provide a measurement technique which would remain useful for an optically thick, highly ionized test gas. Since experimental emphasis was shifted to low density test gases during the project the conductivity

gage was never fully utilized as an independent measurement instrument; it did, however, provide valuable backup measurements to aid in interpreting the optical records.

The original concept of the conductivity gage was simply to apply a voltage across two electrodes in the shock tube walls and measure the dc current through the plasma. A complete theoretical analysis of this concept is presented in Sec. 4.4.1. Experimental results indicated that time-varying effects were of considerable importance in interpreting the record, and the theory was improved to take these effects into account. It was noted that for the experimental conditions under study the magnetic diffusion time was of the same order of magnitude as the test time or, to put it another way, the magnetic Reynolds number was of order unity.

As a consequence the concept of scalar conductivity measurements was drastically modified to eliminate the problems of magnetic diffusion time. Basically, the new concept consists of measuring the scalar conductivity at a frequency high enough that the time variation of the flow is relatively negligible. The high frequency current penetrates only a small distance into the plasma; this "skin depth" can be calculated from the known frequency and the conductivity of the plasma, and is essentially determined by the ratio of magnetic diffusion time to the period of the high frequency current.

The gage is designed to take advantage of this known skin depth to provide a local measurement of stagnation conductivity at the front of the gage. Two versions of the gage are shown in Figs. 2.3 and 2.4. Essentially the gage operates by measuring the shunt impedance presented by the plasma between the inner and outer conductors of a coaxial transmission line. A radio frequency voltage (on the order of 50 to 100 MHz) is applied to one end of this transmission line and the attenuated voltage is measured at the other end of the line. The highly attenuated signal provides a direct measurement of the shunt impedance presented by the highly conductive plasma.

The shunt impedance may be related to the plasma conductivity averaged over the skin depth, which is typically less than a millimeter. A theory describing this relation is presented in Sec. 4.4.2, from which it is deduced that the shunt impedance varies inversely with the square root of the plasma conductivity.

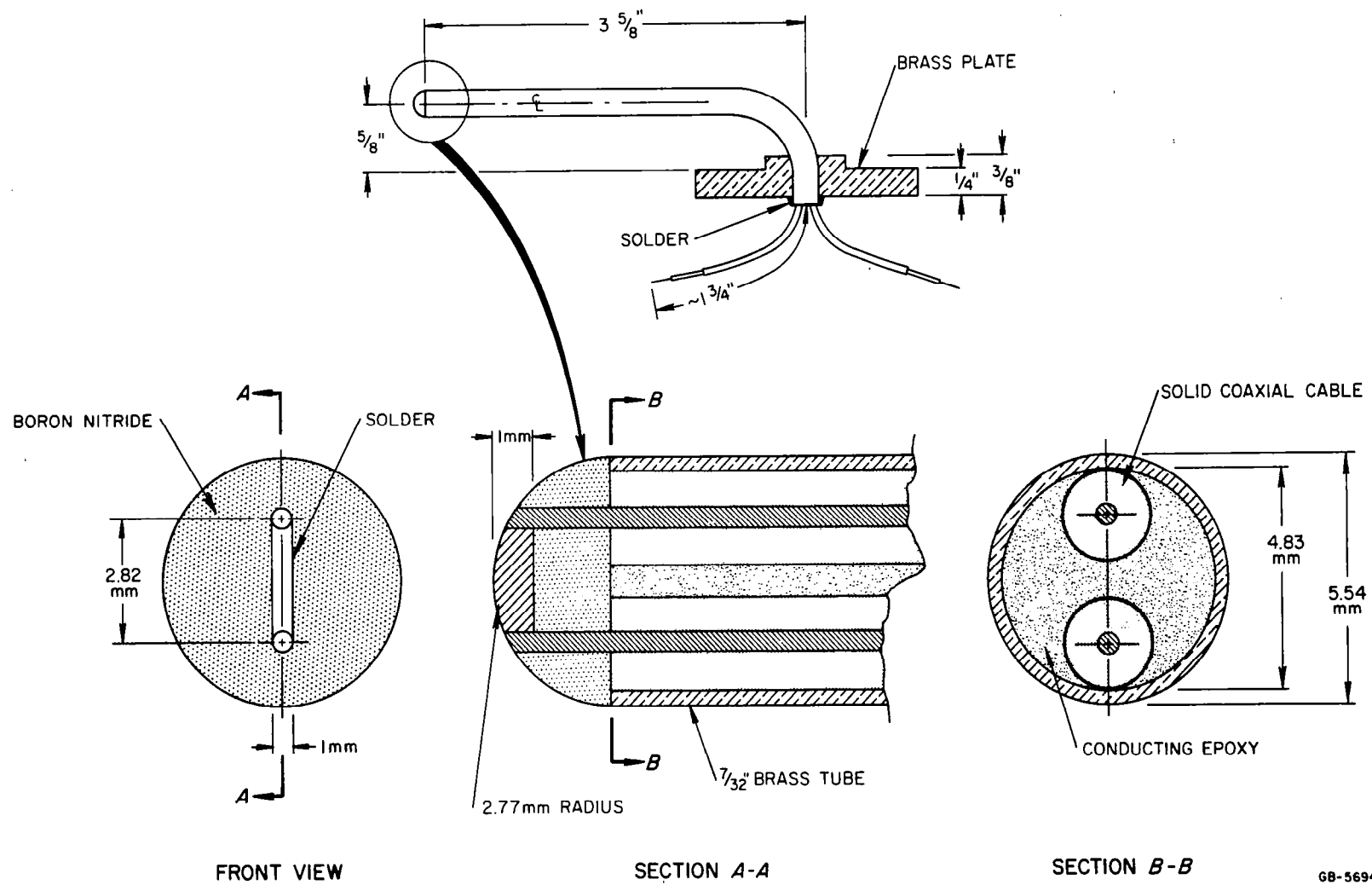
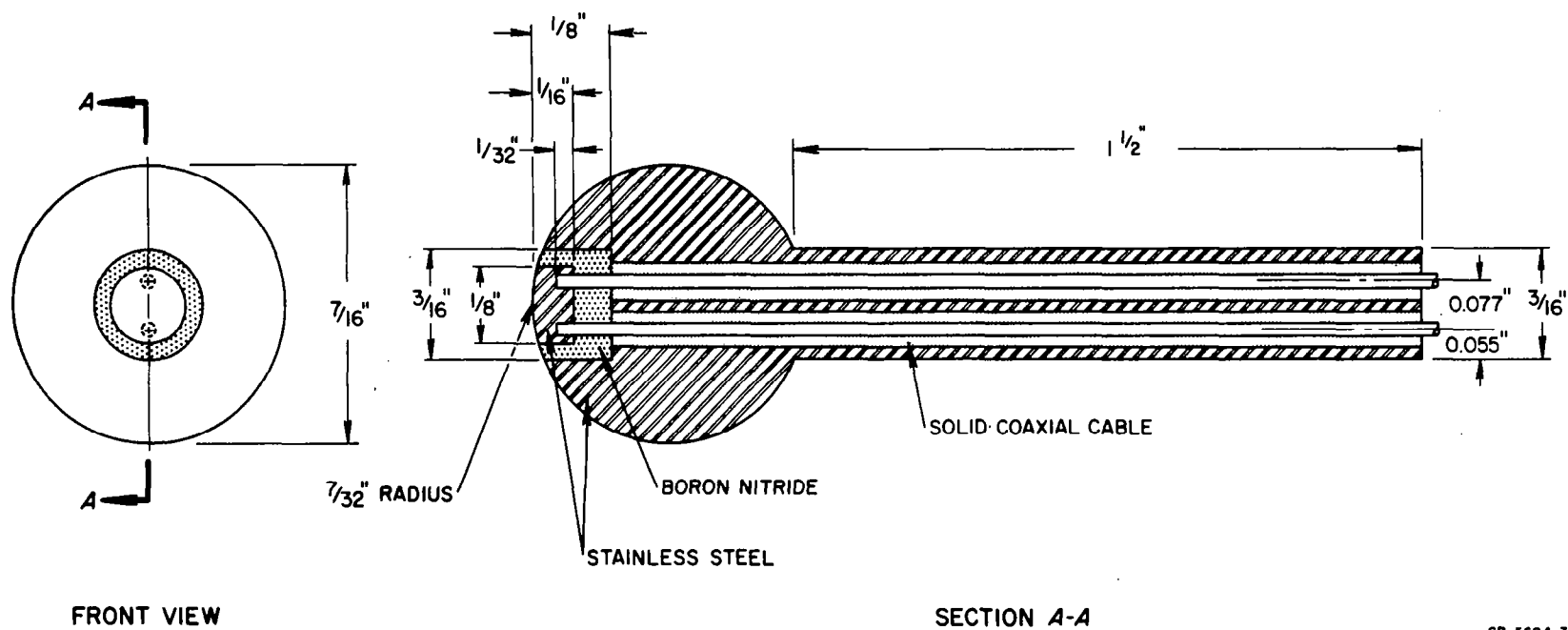


FIG. 2.3 CONDUCTIVITY GAGE A



GB-5694-3

FIG. 2.4 CONDUCTIVITY GAGE B

The conductivity gage measures the stagnation conductivity at the face of the gage and does not, in its present configuration, provide a direct measurement of free-stream properties. It is, however, quite possible to conceive of configurations in which this direct measurement can be made but at the expense of using a more complicated mechanical device.

The basic assumptions underlying the operation of this conductivity gage are: (1) the conductivity is a scalar quantity; and (2) the voltage drop across the plasma sheath is small compared to the voltage drop across the plasma. The first assumption is definitely valid over the range of experimental measurements, and the success of the technique depends upon the adequacy of the second assumption. Unfortunately a detailed calculation of the relative voltage drops was not made during the project, so the assumption was never adequately tested. It should be noted, however, that with appropriate electronic filtering only signals with the proper frequency are measured and the dc voltage drop across the plasma sheath is ignored.

3. EXPERIMENTAL RESULTS

Two different types of implosive drivers—jetting and nonjetting systems—are shown in Fig. 3.1. Configurations A and B depend upon the formation of a diffuse glass jet to drive a shock into the test gas at a velocity approximately equal to twice the explosive detonation velocity. A comparable shock velocity is obtained in Configuration C by first implosively shocking helium by means of a nonjetting driver, and then expanding the shock-compressed and accelerated driver gas through a diaphragm into a low pressure test gas.

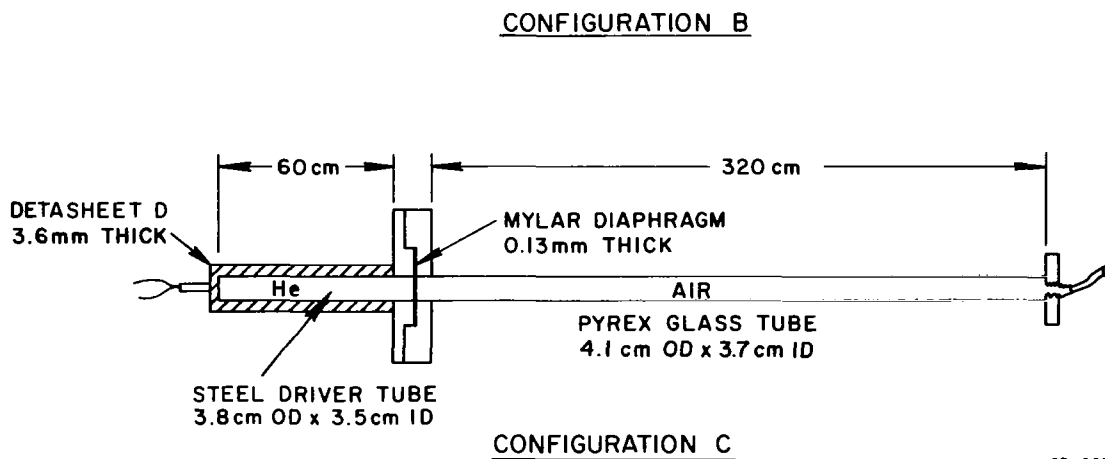
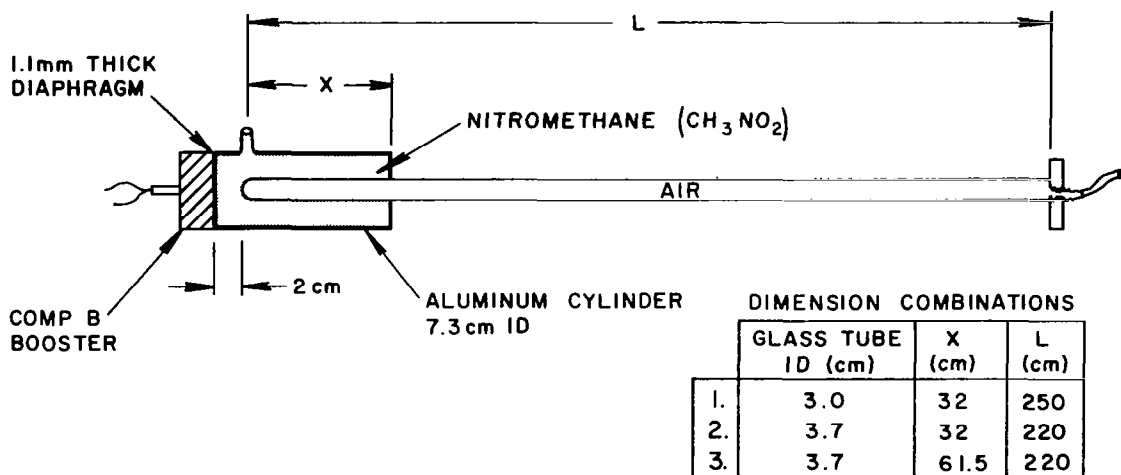
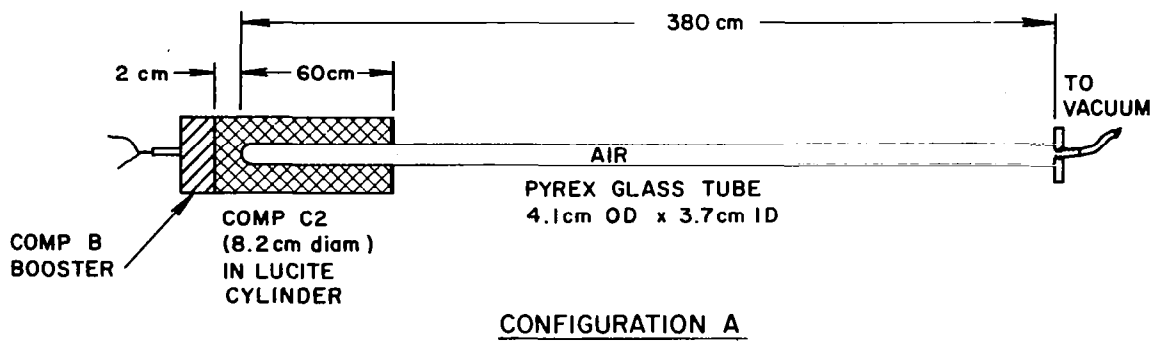
A comprehensive listing of experiments performed during the contract period is presented in Table 3.1. The experiments were designed to optimize the configuration of the implosive driver systems, to test their operating characteristics, and to determine the quality, uniformity, purity, and duration of the resulting high energy test gas flow. In all cases air at initial pressures ranging from 0.5 to 5 torr was chosen as the test gas, and special precautions were taken to dry the air at pressures of 1 torr or less.

3.1 The Jetting Driver

3.1.1 Driver Characteristics

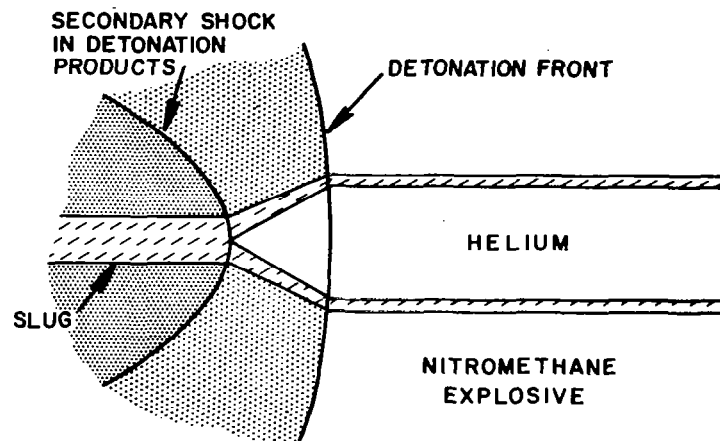
Most of the basic processes and mechanisms involved in the implosive collapse of glass tubes have already been identified and reported in a study by Crosby and Gill²; a flash X-ray of this collapse is shown in Fig. 3.2. Crosby and Gill noted that for a sufficiently high ratio of explosive mass to glass tube mass, on the order of 2:1 or greater, a diffuse glass jet was formed which traveled ahead of the implosive collapse region.

It follows from Birkhoff's theory of jet formation⁶ that the jet has a velocity of twice the explosive detonation velocity, and the jet mass m_j is related to the implosion velocity v and the detonation velocity D by the approximate relation



GB-5694-5

FIG. 3.1 IMPLOSIVE DRIVER CONFIGURATIONS



GP-PLTROOI.68-99

FIG. 3.2 FLASH X-RAY OF THE IMPLOSIVE COLLAPSE REGION

Table 3.1
SHOT RECORD

SHOT NO.	INITIAL CONDITIONS	CONFIGURATION	OBJECTIVE OF SHOT
11,872	5 torr air	B1	Shock velocity and test time history over 2.5 meters.
11,905	5 torr air	B1	DC conductivity measurement and observation of glass slug impact.
11,933	6-7 torr air	B1	Instantaneous shock velocity and test time at 2 meters, emissivity measurement with argon bomb reference.
11,971	5 torr air	B1	Instantaneous velocity and test time at 2.1 meters, emissivity measurement with argon bomb reference, and 50 nsec exposure ICC picture.
11,987	5 torr air	B1 with square shock tube	Instantaneous velocity and test time at 2.2 meters, gas flow characteristics from framing camera record, and emissivity with argon bomb reference.
12,035	5 torr air	B2 with square shock tube	Electronic measurement of average shock velocity and test time.
12,078	5 torr air	B2 with square shock tube	Shock velocity and test time history from 0.4 to 2.1 meters. Emissivity history with argon bomb reference.
12,123	5 torr air	B3	Shock velocity and test time history, conductivity gage measurements of test time.
12,124	5 torr air	B3	Instantaneous velocity and test time at 3.6 meters. Emissivity with argon bomb reference.
12,181	1 atm air	C	X-ray observation of collapse angle of aluminum tube with C/M of 0.29 and 0.35.
12,182	1 atm air	C	X-ray observation of collapse angle of aluminum tube with C/M of 0.29 and 0.35.
12,183	1 atm air	C	X-ray observation of collapse angle of aluminum tube with C/M of 0.40 and 0.43.
12,240	1 atm air	C	X-ray observation of collapse angle of steel tube with C/M of 0.45.
12,241	1 atm air	C	X-ray observation of collapse angle of steel tube with C/M of 0.53.
12,286	5 torr dry air	A	Time-resolved spectrograph and conductivity measurement at 3.7 meters.
12,293	5 torr dry air	A	Detonation velocity of C2 explosive and shock velocity and test time history from 0.6 to 2.3 meters.
12,294	5 torr dry air	A	Instantaneous velocity and test time at 3.6 meters, emissivity with argon bomb reference.
12,419	0.5 torr dry air	A	Instantaneous velocity and test time at 3.5 meters, emissivity with mirror technique, ICC picture.
12,438	0.75 torr dry air	A	Time-resolved spectrograph and 50 nsec exposure ICC picture.
12,452	0.7 torr dry air	A	Gas flow characteristics from framing camera record, emissivity with mirror techniques and argon bomb reference, conductivity measurement.
12,472	0.5 torr dry air	A	Time-resolved spectrograph and 50 nsec exposure ICC picture.
12,473	1 atm He driver into 1 torr dry air	C	Shock velocity and test time history between 1.2 and 2.2 meters
12,481	1 atm He driver into 1 torr dry air	C	Time-resolved spectrograph, conductivity measurement, and 50 nsec exposure ICC picture.

$$\frac{m_j}{m} = \frac{v^2}{4D^2} \quad (3.1)$$

Crosby and Gill have also estimated the implosive wall velocity in terms of the ratio of the explosive charge mass c to the shock tube wall mass m . The resulting expression for the jet mass is

$$\frac{m_j}{m} = \frac{E}{2D^2} \left[\frac{C/M}{RC/M + S + TM/C} \right] \quad (3.2)$$

Here E is the specific kinetic energy released by the explosive, and R , S , and T are parameters tabulated by Crosby and Gill which depend upon the geometrical configuration of the driver. Values for the jet mass and jet density based on these theoretical estimates are shown in Table 3.2. It is assumed in these calculations that the jet uniformly fills the shock tube. The parameter E/D^2 is obtained from handbook data on explosive properties, and is equal to 0.090 for nitromethane and 0.079 for Composition C2.

Table 3.2

THEORETICAL VALUES OF DRIVER JET MASS

CONFIGURATION	JET DENSITY (g/cm ³)	JET MASS (g)
A	0.054	35.3
B1	0.068	15.5
B2	0.042	14.5
B3	0.042	27.9

The cross-sectional energy distribution of the glass jet was studied experimentally (Shot 11,905) by observing the impact of the jet on a shock tube end plate. The terminal end of the shock tube (Configuration B1) was fitted with an aluminum disk, 1/16th inch thick, the outer surface of which was polished to a mirror finish. The projection of a grid image on the polished surface enabled the smear camera to record the free surface movement and jet breakout as a function of time.

Jet arrival and breakout were clearly evident in the record (Fig. 3.3), and close observation reveals even the arrival of the shock in the 5 torr test gas. The breakout profile shows the first arrival occurring near the tube walls, followed within 2.5 μ sec by a diffuse central core. The structure of the jet resembles a set of nested cylinders, with the outer cylinders leading the core.

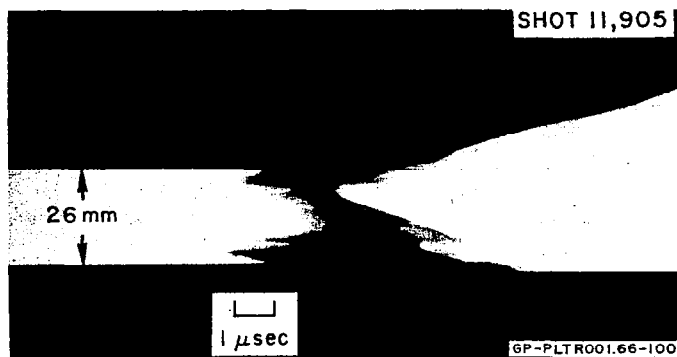


FIG. 3.3 GLASS JET IMPACTING AN ILLUMINATED END PLATE

Another observation indicating the nature of the glass jet was obtained by backlighting the shock tube with an argon bomb. A typical streak camera record (Shot 12,124) presented in Fig. 3.4 shows the strong absorption of the backlight by the diffuse jet. The intensity decrease was measured using standard photometric techniques, and the absorptivity of the glass jet was derived from the relation

$$I/I_0 = e^{-\mu x} \quad (3.3)$$

where I_0 is the backlight intensity, I is the transmitted intensity, μ is the absorptivity, and x is the shock tube diameter.

At a distance of 370 cm from the driver end of the shock tube a value of $\mu = 0.6 \text{ cm}^{-1}$ was found for Configuration B3 (Shot 12,124) using nitromethane explosive, and a value of $\mu = 0.76 \text{ cm}^{-1}$ was found for Configuration A (Shot 12,294) using Comp C2 explosive.

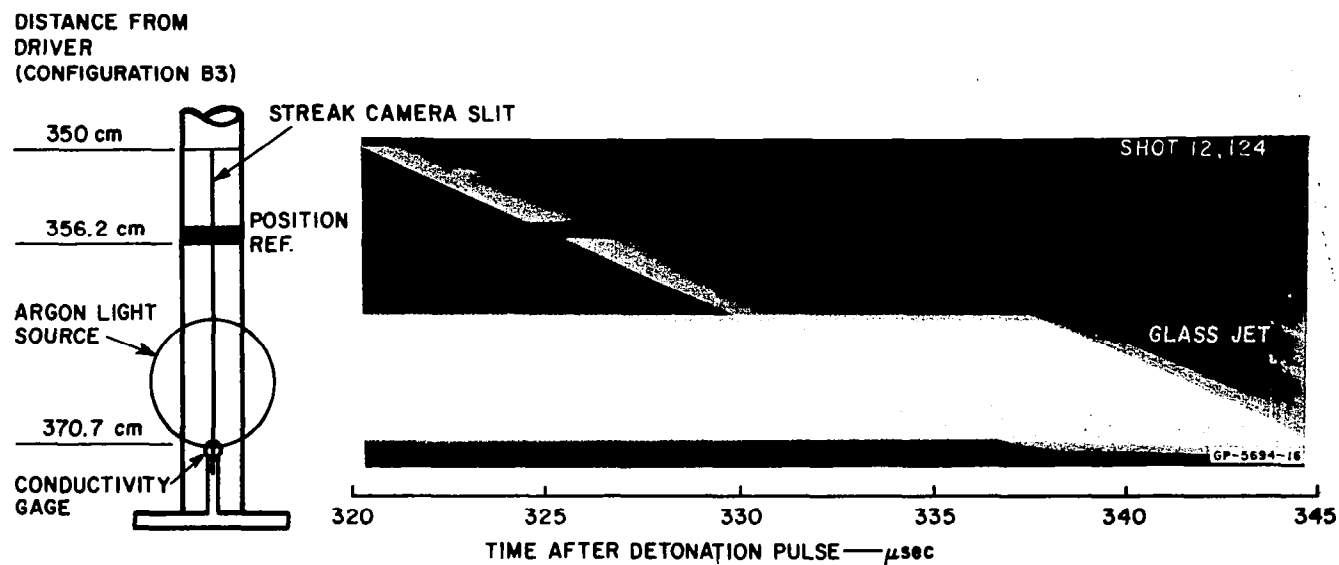


FIG. 3.4 STREAK CAMERA RECORD OF SHOT 12,124

The absorptivity μ is related to the number density n and to the average extinction cross-section S of the glass particles of the jet by the relation

$$\mu = nS \quad (3.4)$$

If we assume the particles to be glass spheres of diameter d , volume V , density ρ_g , and absorption cross-section $S = \pi d^2/4$, we may calculate the mass density of the jet:

$$\rho_j = \mu \rho_g V/S = \frac{2}{3} \rho_g \mu d \quad (3.5)$$

Assuming ρ_j to be the theoretical value (Table 3.2), we obtain an average particle diameter of 404μ for the nitromethane driver and 410μ for the C2 driver, a remarkable correlation considering the approximate nature of the theories involved. The number density of glass particles may be calculated from Eq. (3.4) and the derived particle size; we obtain 480 per cc for the nitromethane driver and 605 per cc for the C2 driver.

3.1.2 Test Gas Flow Properties

3.1.2.1 Shock Velocity

The most accurate technique for measuring the instantaneous shock velocity is to view the axis of the shock tube with a streak camera. In this way a continuous distance-time plot of the luminous shock front and subsequent flow regimes is obtained. A typical streak camera record (Shot 12,123) showing the flow patterns generated by a nitromethane driver, Configuration B3, is shown in Fig. 3.5.

A complicated wave interaction pattern and an abrupt increase in shock velocity from 11.5 to 13 km/sec occur near the driver. In an attempt to determine the cause of this interaction the length of the explosive driver section was doubled from 30 to 60 cm. However, no significant change in the flow pattern resulted from this modification, and the cause of the complex wave interaction pattern remains obscure.

The velocity history of the luminous shock front for both the nitromethane and the C2 drivers is shown in Fig. 3.6. The shock velocity in the nitromethane system starts within 96% of the ideal value based on a jet traveling at twice detonation velocity. Subsequently there is a slow decay in velocity, on the order of 9% over 3.6 meters of shock travel.

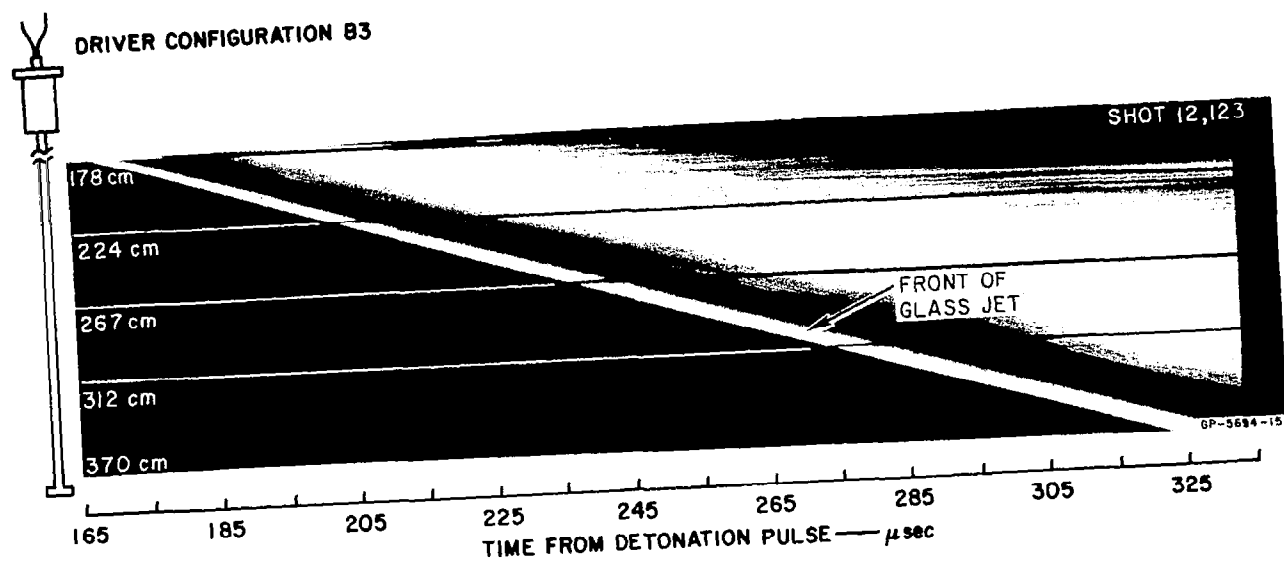


FIG. 3.5 STREAK CAMERA RECORD OF SHOT 12,123

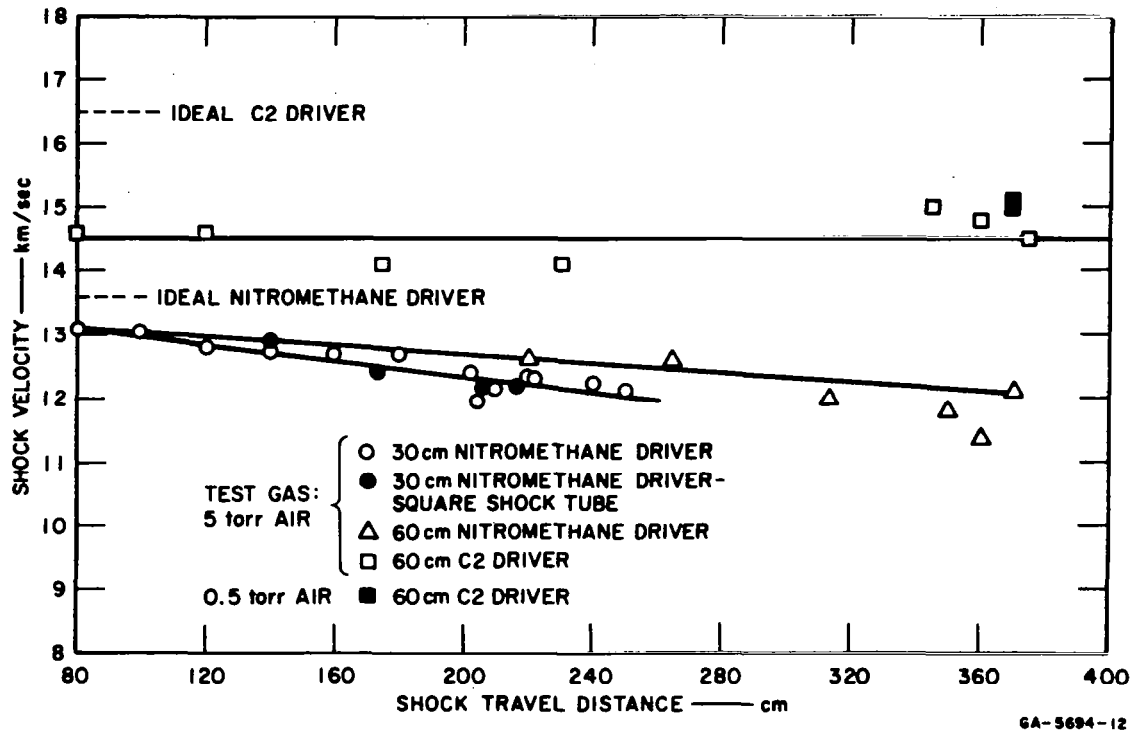


FIG. 3.6 SHOCK VELOCITY vs. TRAVEL DISTANCE FOR THE JETTING DRIVER

The shock velocity in the C2 system starts at 88% of the ideal velocity. The velocity decay of the C2 system is less than that of the nitromethane system, but there are not enough data points to determine the rate of decay.

If the shock velocity decay in the nitromethane system is assumed to be due to the deceleration of the piston, a rough estimate of the mass of the piston can be obtained. We have

$$m \frac{du}{dt} = -A\Delta p \quad (3.6)$$

where m is the piston mass, u the piston velocity, A the cross-sectional area of the shock tube, and Δp the pressure difference across the piston. Assuming that the pressure behind the piston is small compared to the shock pressure (12.6 atm, determined from thermodynamic data), we may estimate the piston mass from the observed velocity decay. In this manner a value of 0.17 g is obtained for the 30 cm driver and a value of 0.32 g for the 60 cm driver.

The fact that the piston mass calculated in this fashion is two orders of magnitude less than the jet mass previously calculated indicates a marked deviation from the assumption of an ideal piston. There are several possible reasons for this behavior, one of the most plausible being that there is a velocity gradient in the jet. Thus, if only a small fraction of the jet is traveling at speeds between 12 and 13 km/sec the mass of the piston calculated above would represent only a fraction of the total piston mass. If this hypothesis were correct, one would expect a decrease of the decay rate of the shock velocity as more of the jet becomes effective as a piston.

3.1.2.2 Duration

The duration of the test gas flow, or test time, was measured using several independent methods. The principal technique, which provides a continuous history of the luminous test time as a function of shock travel distance, is to view the axis of the shock tube with a streak camera, as in Fig. 3.7. The test time was first taken to be the extent of the luminous region, and this measure correlated very well with other techniques

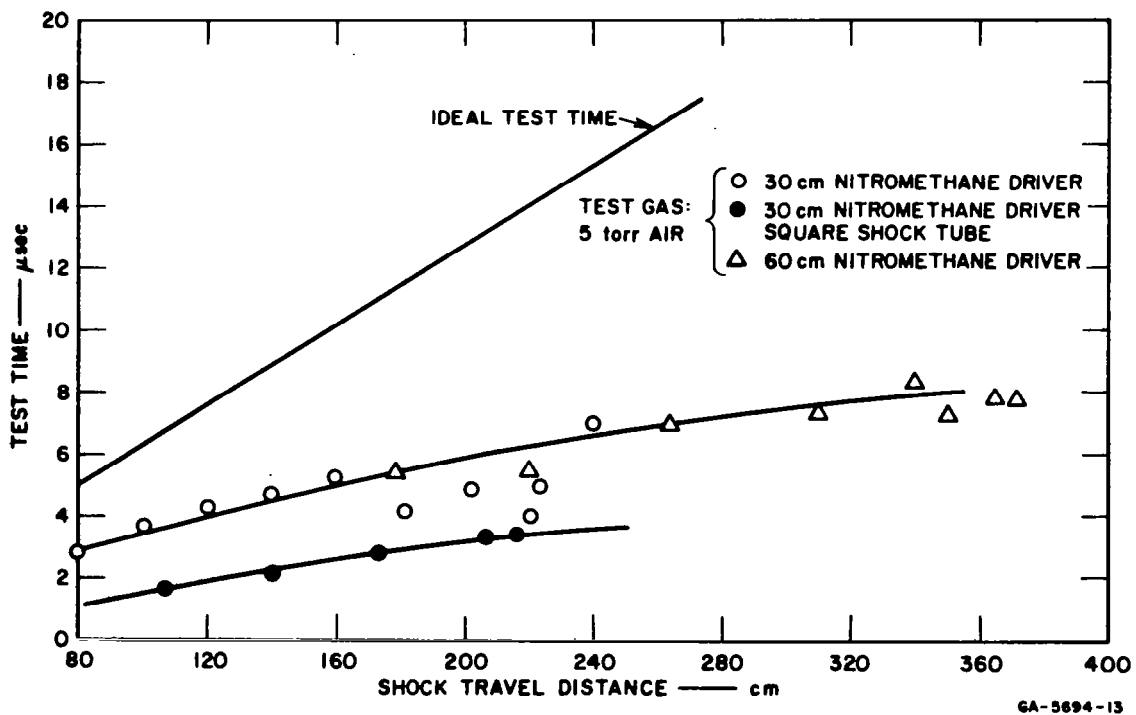


FIG. 3.7 TEST TIME vs. SHOCK TRAVEL DISTANCE FOR THE NITROMETHANE JETTING DRIVER

when the test gas was 5 torr air. For initial pressures less than 1 torr, however, the luminous region did not adequately define the test time, since there was an appreciable decay in intensity behind the shock front.

Other techniques for measuring the test time include backlighting the shock tube and observing the absorption due to the glass jet, directly observing the jet with a framing camera, the conductivity gage record, and the time-resolving spectrograph.

The test time was found experimentally to be sensitive to both the initial test gas pressure and the geometrical configuration of the shock tube. The test times for the nitromethane driver system (Configuration B) and the C2 driver system (Configuration A) are displayed in Figs. 3.7 and 3.8. It is clear that the test times are considerably below the ideal test times with 5 torr air as the test gas, and that transition from the cylindrical driver to a square shock tube (both circumscribing and inscribing the driver tube) leads to a further degradation of available test time. However, for initial pressures less than 1 torr the test time is very nearly equal to the ideal value.

The reason for the pressure sensitivity of the test time has not yet been completely determined. The phenomenon cannot be ascribed to boundary layer mechanisms, as the pressure dependence is the reverse of what would be expected on that basis. A more plausible explanation is that the diffuse glass jet does not act as a perfect piston in driving a shock into the test gas, but acts more like a leaky piston, allowing test gas to flow out of the test region.

In order to quantify the leaky piston concept, let us define the drag of each glass particle in the diffuse jet:

$$D = C_D S \frac{\rho u^2}{2} \quad (3.7)$$

Here C_D is the drag coefficient based on the free-stream conditions behind the shock front, S is the cross-sectional area, ρ is the test gas density, and u is the flow velocity of the test gas relative to the piston. The steady state pressure drop across the piston is then given by

$$\frac{\Delta p}{L} = nD = nSC_D \frac{\rho u^2}{2} \quad (3.8)$$

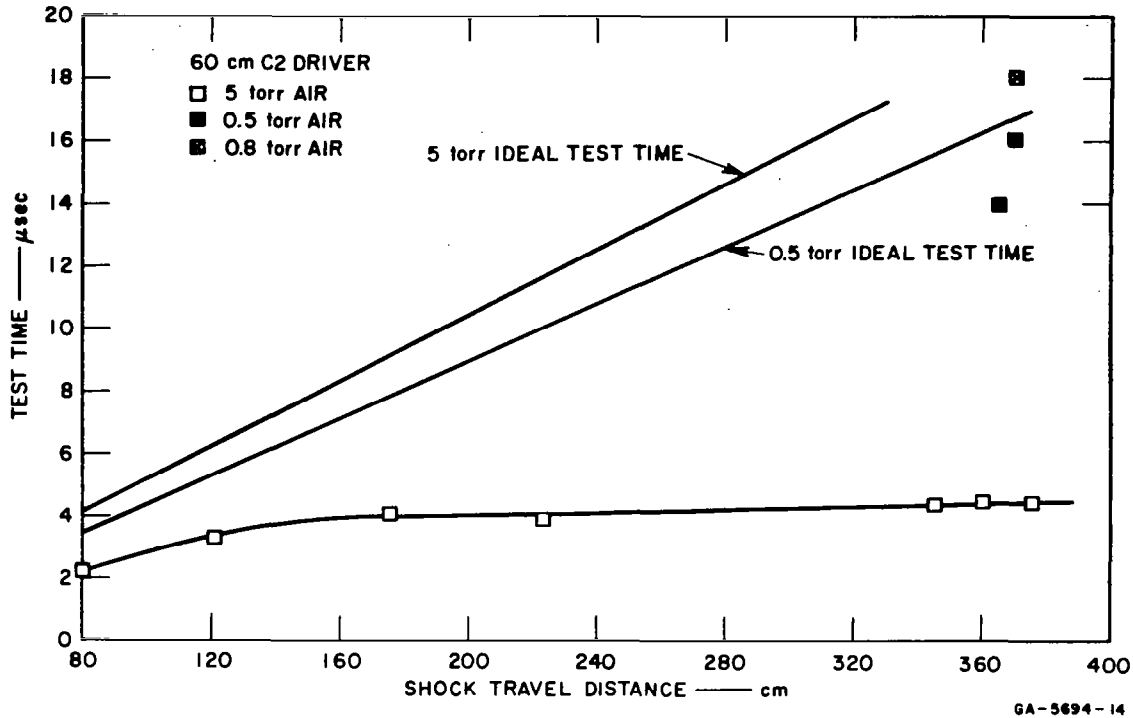


FIG. 3.8 TEST TIME vs. SHOCK TRAVEL DISTANCE FOR THE C2 JETTING DRIVER

If the system has reached its maximum test time, so that all gas flowing through the shock front also flows through the piston, we may calculate the effective value of C_D . Assuming that the shock pressure is much greater than the pressure at the rear of the piston, we can evaluate all quantities in Eq. 3.8 in terms of the absorptivity $\mu = nS$ (see Eq. 3.4), the shock density ratio η , and the piston length L :

$$C_D = \frac{2(\eta - 1)}{\mu L} \quad (3.9)$$

It follows that $C_D = 0.72$ for the nitromethane driver and $C_D = 0.58$ for the C2 driver, both driving air initially at 5 torr pressure.

These values correlate well with the values calculated from Stokes law for the drag of a sphere at low Reynolds numbers:

$$C_D = \frac{24}{\text{Re}} \quad (3.10)$$

The Reynolds number is defined in terms of the kinematic viscosity ν of the test gas and the diameter d of the particles by the relation

$$\text{Re} = \frac{ud}{\nu} \quad (3.11)$$

Assuming the free-stream conditions to be unmodified by the presence of the jet particles, the Reynolds number is 17.2 for the nitromethane driver and 16.1 for the C2 driver. The Stokes law drag coefficients corresponding to these Reynolds numbers are 1.4 and 1.5, respectively.

Schlichting's experimental data⁷ on the drag coefficients of smooth spheres indicate a somewhat higher value for C_D than does Stokes law; the drag coefficients corresponding to the Reynolds numbers of the nitromethane and C2 drivers are 2.7 and 2.8, respectively.

The ratio between the drag coefficients determined from the experimental data and the drag coefficients calculated according to Stokes law or Schlichting's data is on the order of 2 to 4. This difference is small compared to the uncertainty of the assumptions concerning the jet particles and the stream conditions, and provides encouraging support for the theory. The agreement can be improved considerably by assuming an n -fold density increase due to radiative and conductive cooling of the test gas as it passes through the jet; the experimental drag coefficient based on Eq. (3.7) would then be increased proportionately (by a factor of n) to provide a drag coefficient based on local free-stream conditions.

The growth of test time is related to the difference between mass influx through the shock and mass efflux through the piston by the equation

$$\frac{d\tau}{dx} = \frac{\dot{M}_s - \dot{M}_p}{(\eta - 1)\rho_1 U_s^2} \quad (3.12)$$

Here \dot{M}_s is the mass flux through the shock, \dot{M}_p is the mass flux through the piston, τ is the test time, and x is the shock travel distance. From Eq. (3.8), assuming that the pressure at the rear of the piston is negligible, we have

$$C_D \mu \frac{\rho u^2}{2} = \frac{\eta - 1}{\eta L} \rho_1 U_s^2 \quad (3.13)$$

This equation may be solved for the mass flux ρu through the piston:

$$M_p = \frac{2(\eta - 1)}{(C_d u) \eta \mu L} \rho_1 U_s^2 \quad (3.14)$$

The growth in test time is then given by

$$\frac{d\tau}{dx} = \frac{1}{(\eta - 1)U_s} - \frac{2}{\eta \mu L (C_d u)} \quad (3.15)$$

The ratio \dot{M}_p / \dot{M}_s was calculated from Eqs. (3.13) and (3.14), using Schlichting's data on the drag of smooth spheres, and is plotted in Fig. 3.9. The equations had to be solved iteratively, since the drag coefficient depends on the Reynolds number, which in turn depends upon the velocity u .

It is clear from these calculations that the effectiveness of the diffuse jet as a piston is greatly augmented at low pressures, and this conclusion is borne out by the observed increase in test time at

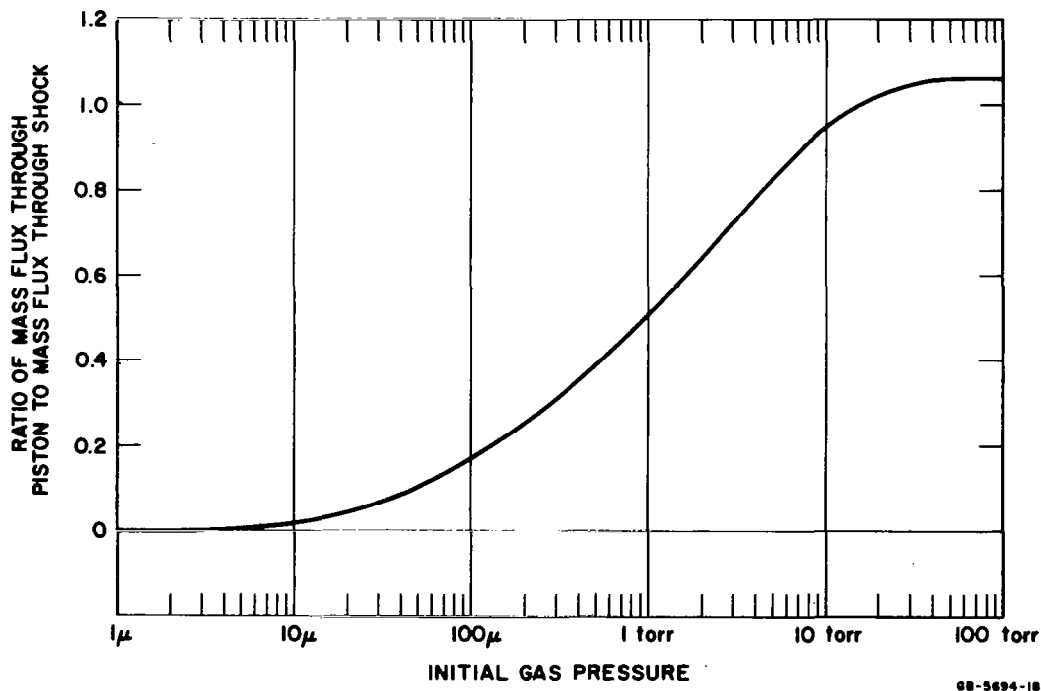


FIG. 3.9 MASS FLUX THROUGH THE DIFFUSE PISTON AS A FUNCTION OF INITIAL AIR PRESSURE

pressures less than 1 torr to the ideal maximum test time. The reason for the augmented effectiveness is seen to be the increase in drag coefficient of the individual jet particles at low Reynolds numbers, which would imply that the driver could be made more effective at a given jet density by decreasing the average particle size and increasing the number density of particles.

3.1.2.3 Uniformity

The planarity of the shock front and the cross-sectional uniformity of the test gas were determined principally from framing camera photographs. A sequence showing the flow around a hemispherical conductivity gage, (Type A, Fig. 2.3) is shown in Fig. 3.10. A nitromethane driver (Configuration B2) was butt-joined into a square aluminum shock tube containing 5 torr air, and the flow was viewed by a Schlieren optical system through two optically flat windows. The sequence clearly shows the flat shock front—no detectable curvature is present—and the uniform flow around the gage. No turbulence or nonuniformity is evident in the flow until the glass jet comes into view 3.5 μsec after the shock front.

A similar sequence (Fig. 3.11) showing the flow around the conductivity gage B (Fig. 2.4) produced by the C2 driver (Configuration A) in 0.7 torr air indicates the increase in performance at low pressures. The

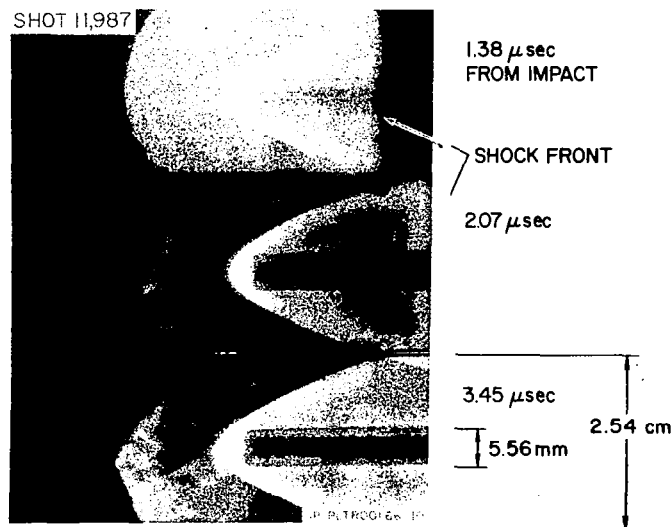


FIG. 3.10 FLOW AROUND CONDUCTIVITY GAGE A

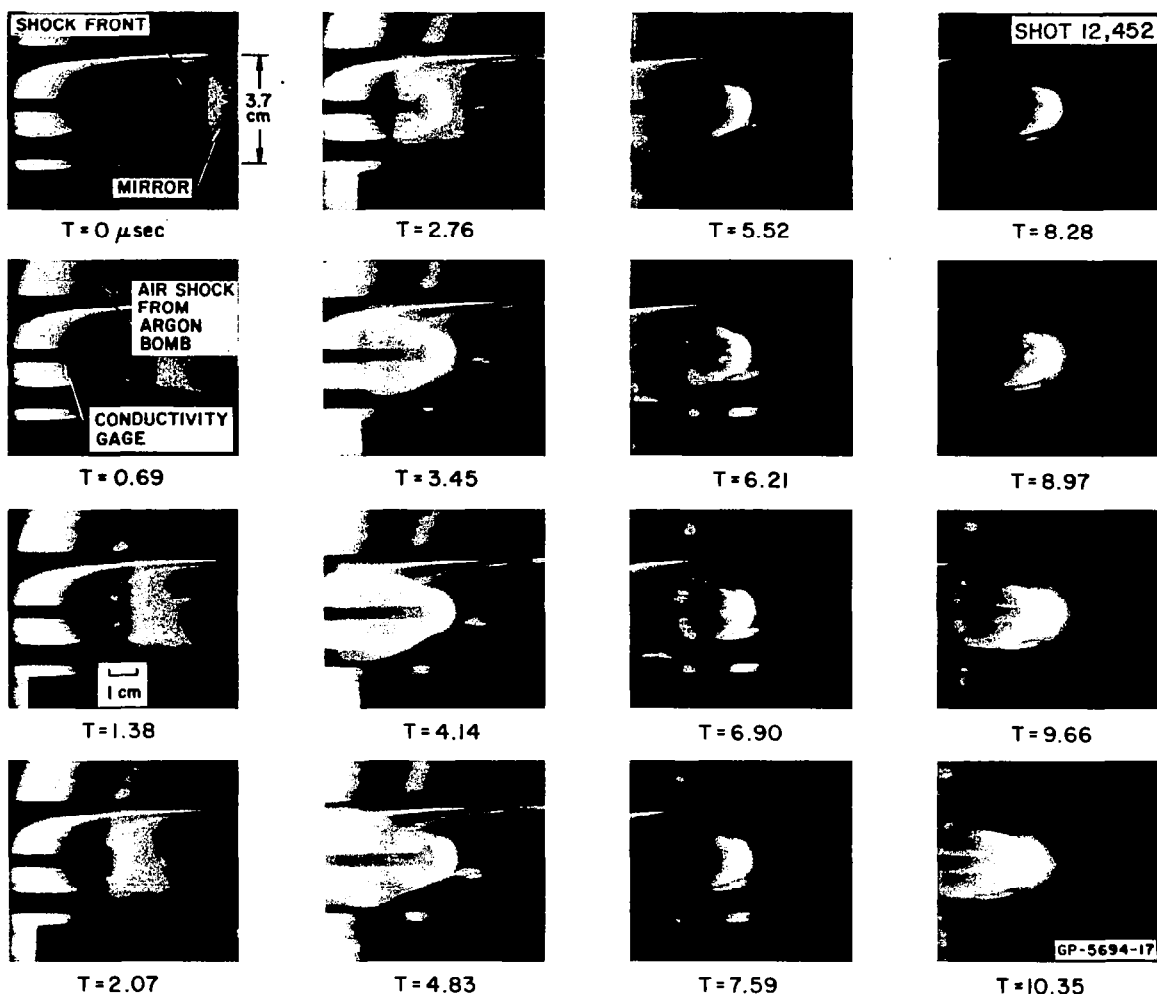


FIG. 3.11 FLOW AROUND CONDUCTIVITY GAGE B

optical system for this sequence is not nearly so favorable as it was for the previous photographs. The self-luminous flow is viewed through the irregular walls of a 41 mm OD Pyrex tube, and severe optical distortions are evident. In addition, the light produced by an air blast is visible behind the shock tube. In spite of these optical difficulties the uniform, high quality nature of the test gas flow is evident for at least 11 μsec after shock front arrival.

The uniformity and duration of the flow are also evident in the rf conductivity gage records (Fig. 3.12). The conductivity, which is inversely proportional to the square of the rf voltage (see Sec. 2.3), is seen to decrease slowly behind the shock front.

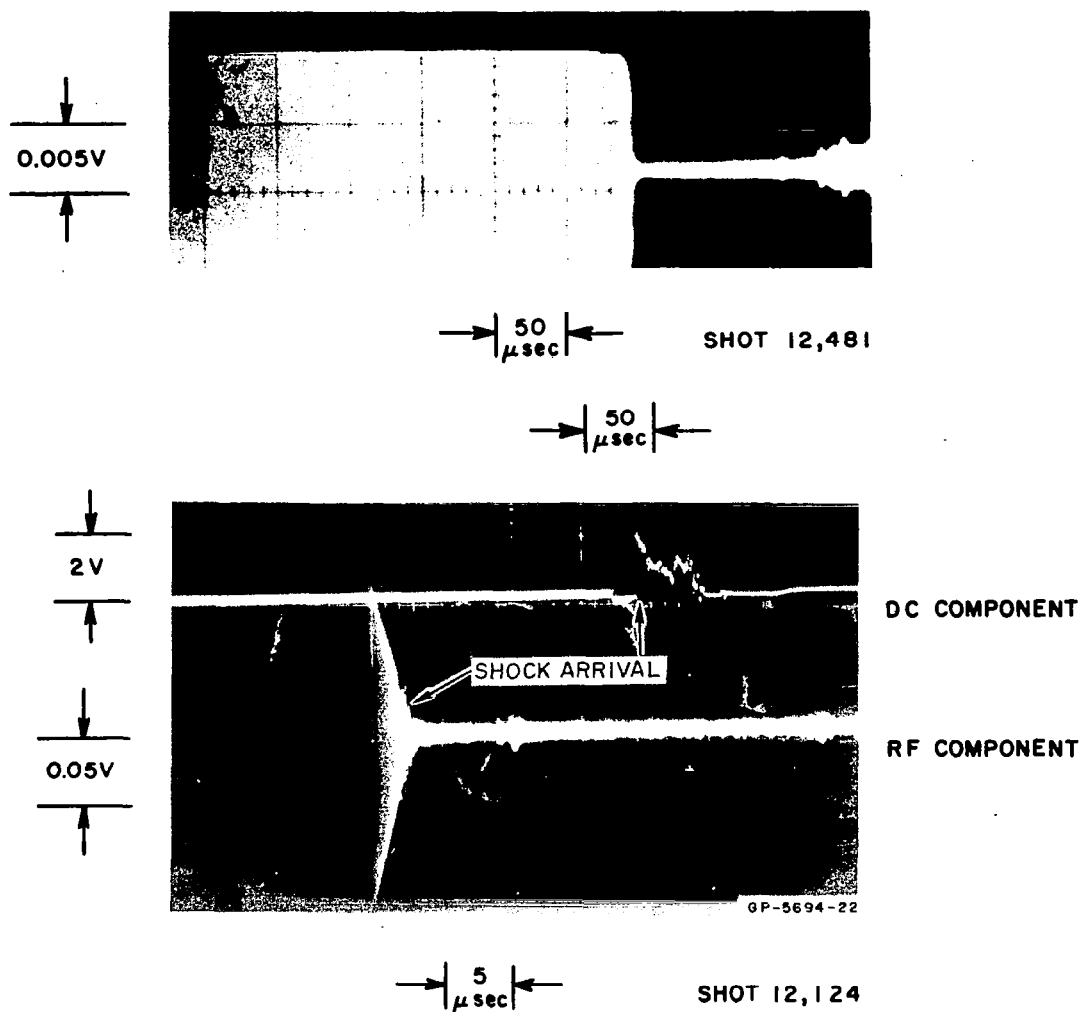


FIG. 3.12 RF CONDUCTIVITY GAGE RECORDS

3.1.2.4 Purity

The chemical purity of the test gas flow was determined by spectrographic observations of the radiating gas. A selection of these spectral records is shown in Figs. 3.13 and 3.14. Strong radiative cooling is evident in the records, as is line emission from hydrogen and sodium contamination in the original test gas. The distinctive radiation from the diffuse glass jet is clearly defined, however, and there is no appreciable mixing of driver contaminants with the test gas. The spectrographic test times agree closely with the test times obtained by measuring the extent of luminous emission in both framing and streak camera records.

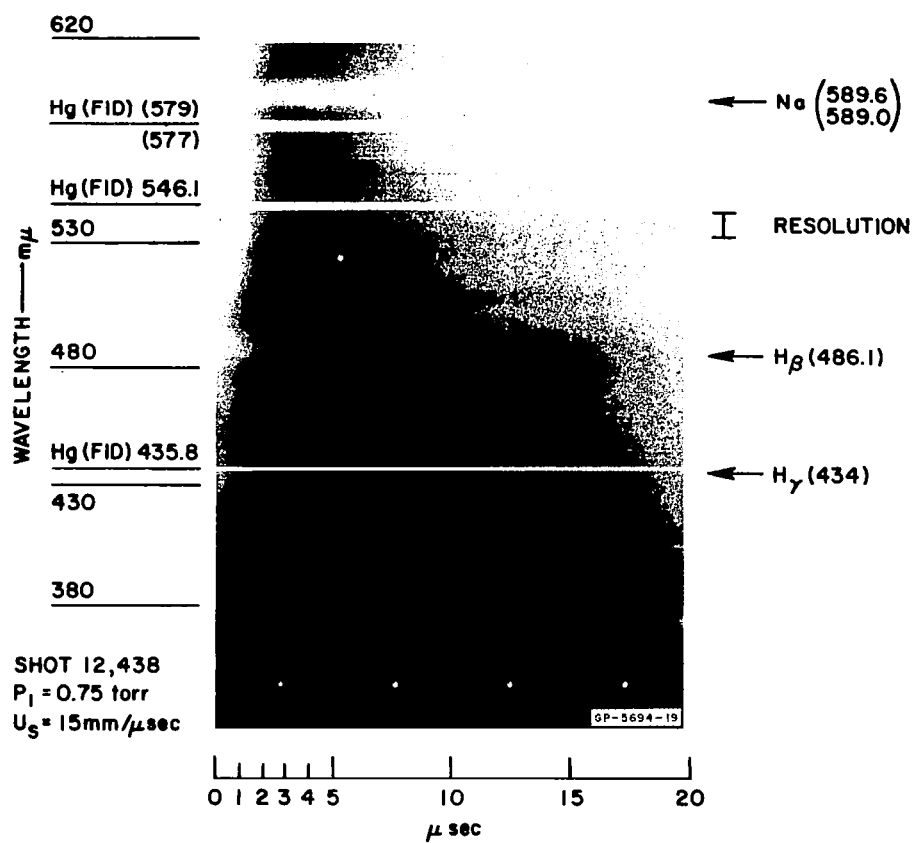


FIG. 3.13 TIME-RESOLVED SPECTROGRAPH OF SHOT 12,438

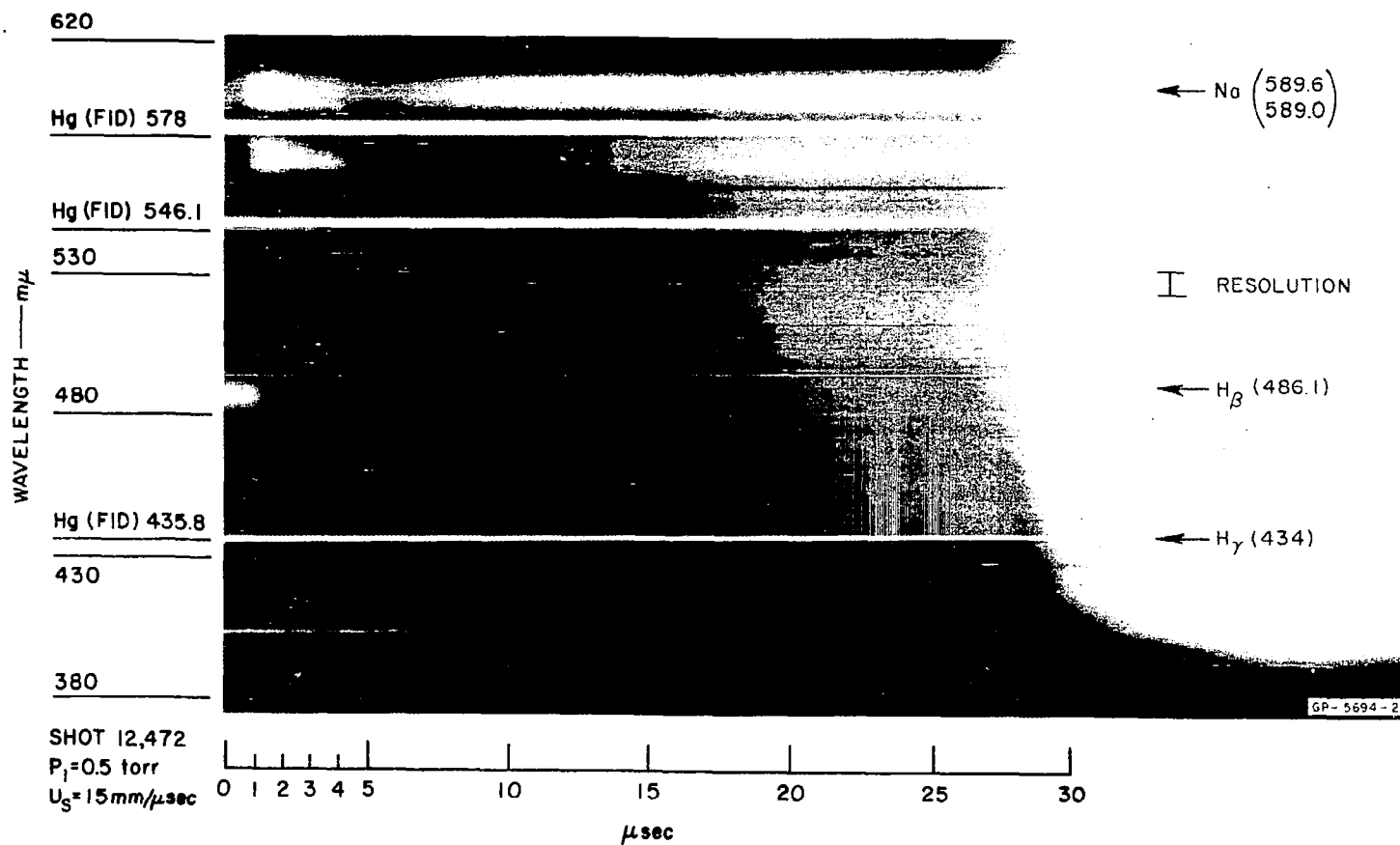


FIG. 3.14 TIME-RESOLVED SPECTROGRAPH OF SHOT 12,472

3.1,2,5 Gas Properties

In the course of investigating the characteristics of impulsively driven shocks a certain amount of quantitative data on the temperature, absorptivity, conductivity, and electron density of high temperature air was obtained. However, these measurements were not intended to provide primary data on the thermodynamic and radiative properties of high temperature air, but rather to provide supplementary information on flow uniformity and duration. The policy of emphasizing the measurement of flow properties rather than gas properties led in several cases to sacrificing accuracy and unambiguity in order to achieve the necessary time resolution of the data. It is, of course, entirely possible to obtain data of much greater accuracy, and this effort is suggested in Sec. 6 as a possible future research project with the implosive shock tube.

Whenever possible, the streak and framing camera records were used to determine the emissivity and temperature of the high energy test gas flow. The results of these measurements in dry air at various initial pressures are shown in Table 3.3. The results are necessarily crude because of the wide spectral range of the measurement. This range was chosen to provide adequate film density at the short exposure times employed (on the order of 100 nsec). Because of a variety of problems with timing and exposure, only one shot provided sufficient information to perform an accurate temperature measurement. The measured temperature was found to be close to the value calculated from the thermodynamic properties of air.

Table 3.3

EXPERIMENTALLY DETERMINED EMISSIVITY AND TEMPERATURE

SHOT NUMBER	PRESSURE (torr)	TUBE DIAMETER (cm)	u_s (km/sec)	TEMPERATURE °K	EMISSIVITY	ABSORPTIVITY (cm ⁻¹)
11,933	6.5 ± 0.5	2.6	11.9	14,370 ± 200 ^a	0.73 ± 0.08 ^b	0.50 ± 0.05 ^c
11,971	5.0 ± 0.1	2.6	12.1	14,630 ± 100 ^a	0.61 ± 0.04 ^b	0.36 ± 0.03
12,078	5.0 ± 0.1	2.54	12.2	14,790 ± 100 ^a	0.80 ± 0.05 ^b	0.63 ± 0.04
12,124	5.0 ± 0.1	3.7	11.3	13,590 ± 100 ^a	0.41 ± 0.03 ^b	0.14 ± 0.01
12,419	0.5 ± 0.1	3.7	15.1	15,200 ± 100 ^a	0.62 ± 0.01 ^b	0.26 ± 0.004
12,452	0.7 ± 0.1	3.7	15.3	16,000 ± 100 ^a	0.44 ± 0.01 ^c	0.16 ± 0.004
				15,250 ± 350 ^d		

^a. Temperature taken from thermodynamic charts.

^b. Argon bomb reference technique.

^c. Mirror technique.

^d. Temperature measured experimentally using an argon bomb reference source.

^e. Limits of known experimental errors are indicated.

The experimental values for the absorptivity of the test gas behind the shock front do not agree favorably with the thermodynamic calculations (as can be seen by referring to Fig. 4.1). On the other hand, the temperature, which is calculated from the measured value of emissivity, falls very close to the thermodynamic calculations. Also it was noted that whenever it was possible to measure the emissivity of the gas using several of the techniques described in Sec. 2.2, the measured values agreed within experimental error limits. Thus it is believed that much of the observed discrepancy between the calculated thermodynamic values and the measured values of the absorptivity is real.

W. A. Page of NASA-Ames has analyzed the records from the time-resolving spectrograph⁸ and has obtained a direct measure of the electron density in the test gas as a function of position behind the shock front from the observed widths of the Stark-broadened H_β and H_γ lines. This measured electron density profile correlates very well with the values computed from the equilibrium thermodynamic properties of high temperature air and calculated values of the radiative cooling of the test gas.

3.2 Jetless Driver

The jetless driver (Configuration C) is used to drive a shock tube in a manner closely resembling a conventional shock tube. Helium driver gas, initially at 1 atm pressure, is shock-heated, compressed, and accelerated to a velocity of 7.2 km/sec by the implosive collapse of the driver tube. The helium then bursts a thin Mylar diaphragm and expands into low pressure air.

Although this two-gas system provides significant performance capabilities in terms of the ultimate shock velocity in the test gas, it is seriously limited in available test time by boundary layer phenomena. As a consequence, the two-gas system was studied only briefly during this project.

The experimental results correlate very well with the Roshko-Mirels theory of boundary layer leakage.* The luminous test time at a shock velocity of 11.5 ± 0.5 km/sec derived from a streak camera record and the test time taken from a spectrographic record are shown in Fig. 3.15. The value for β , a boundary layer thickness parameter appearing in the Roshko

* See Section 4.2.1.

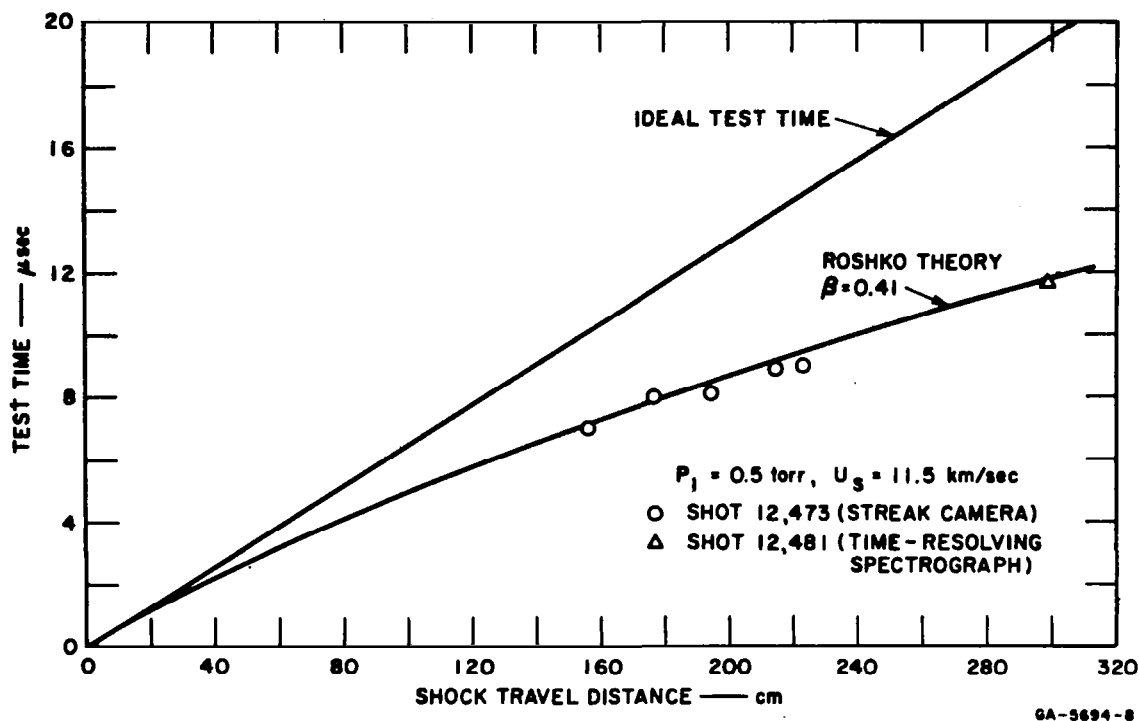


FIG. 3.15 TEST TIME vs. SHOCK TRAVEL DISTANCE FOR THE JETLESS DRIVER

theory, was chosen to fit the data. Graphical extrapolations of Kemp's calculations* to the high temperatures achieved in the experiment indicate a value for β of approximately 0.64, which would lead to a significantly lower test time than was in fact achieved.

The time-resolved spectrograph record, Fig. 3.16, indicates that the test gas flow is free of contamination from the helium driver gas. Both the spectrograph record and the test time results indicate that the two-gas system is free of much of the interface mixing between driver gas and test gas that is characteristic of the operation of conventional shock tubes.

* See Section 4.2.1.

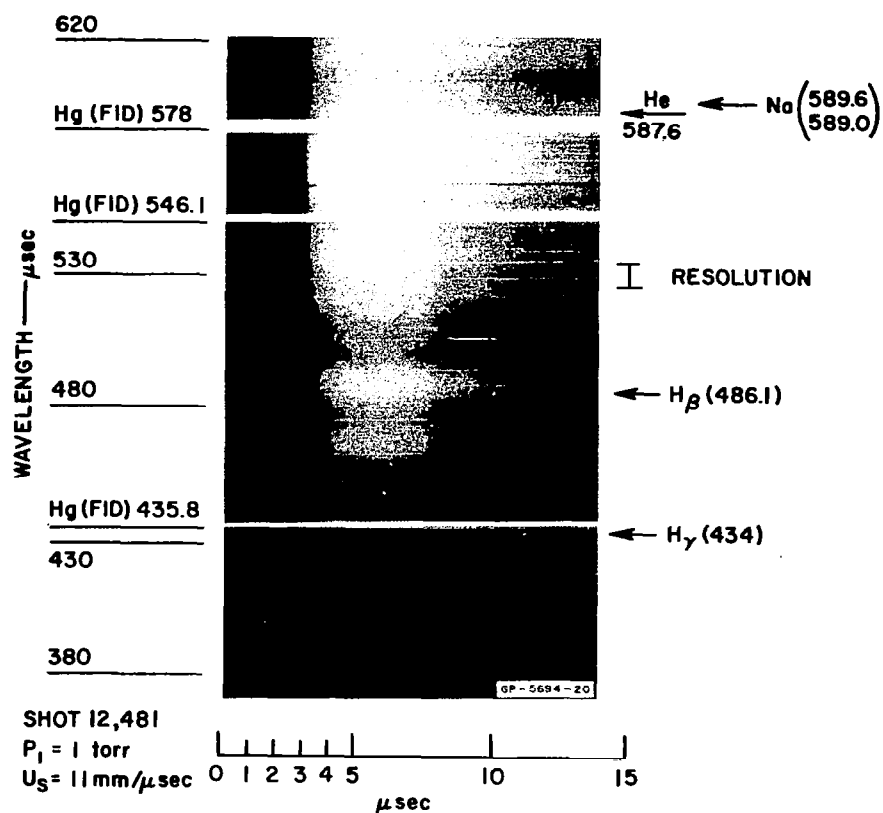


FIG. 3.16 TIME-RESOLVED SPECTROGRAPH OF SHOT 12,481

4. THEORETICAL CALCULATIONS

4.1 Properties of High Temperature Air

A literature search was conducted during this project to obtain reliable, consistent, and reasonably accurate tabulations of calculated thermodynamic, radiative, and transport properties of high temperature air. From the available data an enthalpy-pressure chart of the equilibrium thermodynamic state properties was prepared, and various overlays representing radiative properties and solutions to the Hugoniot shock equations were constructed (Fig. 4.1).

4.1.1 Thermodynamic Properties

The literature search was facilitated by a recent critical review of the data on the thermodynamic properties of high-temperature air by Kuthe.⁹ From the few reliable sources of data on air at temperatures exceeding 10,000°K the work of Fenter and Gibbons¹⁰ was chosen as the most recent, comprehensive, and adequately documented source of thermodynamic data covering the expected range of experimental conditions.

Fenter and Gibbons consider air whose initial composition (in mol percent) is 78.0881 N₂, 20.975 O₂, and 0.9324 A. They neglect intermolecular interaction and radiation effects, but consider in detail the chemical equilibrium for a system composed of the 30 chemical species N₂, N₂⁺, NO, NO⁺, O₂, O₂⁺, N, N⁺, N²⁺, N³⁺, N⁴⁺, N⁵⁺, O⁻, O, O⁺, O²⁺, O³⁺, O⁴⁺, O⁵⁺, O⁶⁺, A, A⁺, A²⁺, A³⁺, A⁴⁺, A⁵⁺, A⁶⁺, A⁷⁺, A⁸⁺, and e⁻. The thermodynamic functions for each species are calculated by means of partition functions based on spectroscopically determined energy levels. The equilibrium composition of the mixture is determined by numerically solving the chemical equilibrium equations.

Their data are presented as curves of constant temperature, density, and entropy on an enthalpy-pressure diagram. A portion of these data covering the range of experimental interest is presented in Fig. 4.1.

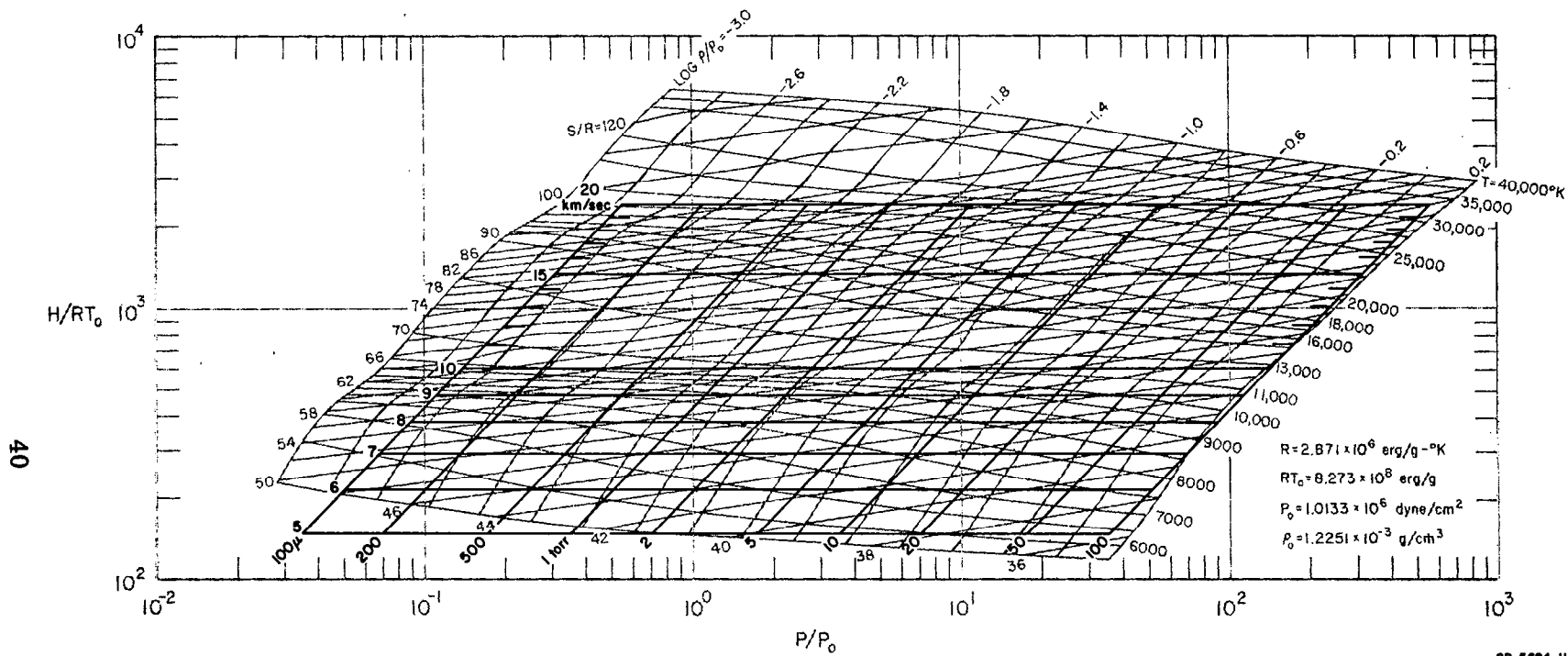


FIG. 4.1A THE THERMODYNAMIC PROPERTIES OF HIGH TEMPERATURE AIR

Note: A colored overlay used to present the radiative properties in the original contractor's report has been deleted from this report to permit black and white reproduction. The radiative data are presented in chart form in fig. 4.1B.

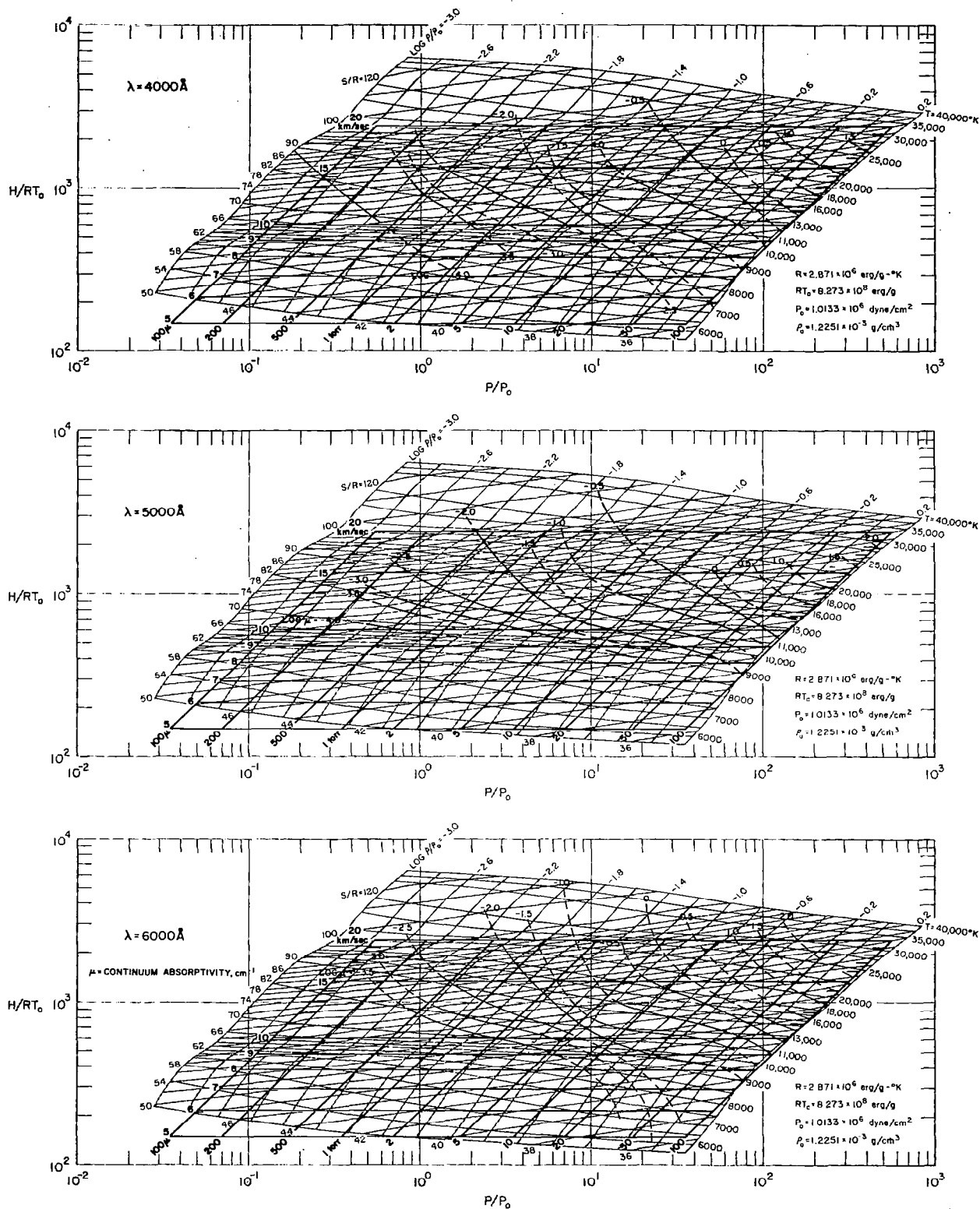


FIG. 4.1 B THE THERMODYNAMIC AND RADIATIVE PROPERTIES OF HIGH TEMPERATURE AIR

4.1.2 Shock Calculations

The enthalpy-pressure diagram of the thermodynamic properties is particularly useful for shock tube work, as the thermodynamic states corresponding to constant shock velocity or constant initial pressure are approximately straight lines. This is easily seen to be a consequence of the conservation laws of mass, momentum, and energy across the shock front:

$$\rho_2 (U_S - u) = \rho_1 U_S \quad (4.1)$$

$$p_2 = p_1 + \rho_1 u U_S \quad (4.2)$$

$$\rho_1 U_S \left(e_2 + \frac{1}{2} u^2 - e_1 \right) = p_2 u \quad (4.3)$$

Here U_S is the velocity of the shock front moving into stationary gas, and u is the particle velocity of the shocked gas. The subscript 1 refers to the unshocked gas and the subscript 2 refers to the shocked gas. The thermodynamic properties entering into the conservation laws are the pressure p , the density ρ , and the specific internal energy e .

We may solve Eq. 4.1 for the ratio of particle velocity to shock velocity in terms of the density ratio across the shock:

$$u = \mu U_S \quad (4.4)$$

where

$$\mu = 1 - \rho_1 / \rho_2 \quad (4.5)$$

The enthalpy

$$h = e + p/\rho \quad (4.6)$$

and the pressure of the shocked gas are readily obtained in terms of the parameter μ :

$$p_2 = p_1 + \mu \rho_1 U_S^2 \quad (4.7)$$

$$h_2 = h_1 + \mu(2 - \mu) U_S^2 / 2 \quad (4.8)$$

Over the expected range of experimental conditions p_1 is negligible compared to p_2 , h_1 is negligible compared to h_2 , and the density ratio ρ_2/ρ_1 varies between 10 and 20. As a consequence μ is nearly constant, varying between 0.9 and 0.95. The shock enthalpy is even more precisely

determined, with $\mu(2 - \mu)$ varying between 0.99 and 0.9975. Thus at a given shock velocity the specific enthalpy h_2 is very nearly constant and independent of the initial density ρ_1 . The ratio between the shock pressure and enthalpy is given by

$$\frac{p_2}{h_2} = \frac{2}{(2 - \mu)} \rho_1 \quad (4.9)$$

and is therefore linearly dependent on the initial density, but is independent of the shock velocity.

To calculate the exact value of the density ratio ρ_2/ρ_1 and to determine values of the other thermodynamic functions such as temperature and entropy, we construct two straight lines on an enthalpy-pressure chart of the thermodynamic properties. The first line is the constant enthalpy line corresponding to the given value of the shock velocity, and the second is the straight line defined by Eq. 4.9 whose slope is determined by the initial density. The point at which these two lines cross satisfies both equations and determines the thermodynamic state of the shocked test gas.

The value of ρ_2 read from the thermodynamic chart can be used to update μ and refine the point of intersection of the curves, but this refinement is less than the graphical accuracy of the chart for values of ρ_1/ρ_2 in the range 10 to 20.

An overlay displaying these curves for various shock velocities and initial densities has been constructed and is presented in Fig. 4.1. The thermodynamic state of the shocked gas is determined by the point of intersection of the lines corresponding to the appropriate initial pressure and shock velocity.

4.1.3 Radiative Properties

Several tabulated calculations of the radiative properties of high temperature air in thermal equilibrium have appeared in the literature, but to the authors' knowledge there has been no critical review of the accuracy and consistency of these calculations. For the purposes of this project the work of Sewell, Fenter, and Gibbons¹¹ was chosen as the source of data. In addition to being a highly respected set of calculations of the radiative properties of high-temperature air, the work has

the advantage of being based on the equilibrium thermodynamic data of Fenter and Gibbons,¹⁰ and thus provides a certain amount of consistency between the calculated thermodynamic and radiative properties.

An overlay chart of the continuum optical absorptivity at 4000Å, 5000Å, and 6000Å as a function of thermodynamic state has been constructed from the data and is presented in Fig. 4.1. Due to the paucity of calculated points in the thermodynamic region of interest the interpolation and extrapolation of data are necessarily crude. The extrapolated points which are particularly doubtful in the estimation of the author are represented by dashed lines.

The calculated absorptivity values represent only the continuous spectrum, and the contributions of the line spectrum are neglected.

4.2 Boundary Layer Effects

4.2.1 Two-Gas System

The effects of boundary layer growth on the performance of a two-gas system should be similar to those of a conventional shock tube driver. In both cases a compressed and heated driver gas bursts a diaphragm and expands into a low pressure test section, driving a shock into the test gas. A boundary layer forms in the test gas at the shock tube wall, and this layer of low velocity, high density gas provides a leakage path for the test gas around the contact surface.

This mass flow around the interface is readily visualized by considering the boundary layer in a coordinate frame fixed with respect to the contact surface. In this frame of reference the flow in the boundary layer is seen to be a flow out of the region between the shock front and the interface.

This mass flow of test gas around the interface is a dominant effect, leading to severe limitation of the test time in conventional shock tubes. It has been treated theoretically by Anderson,¹² Roshko,¹³ and Mirels,¹⁴ who found reasonable agreement with the data from low speed shock tubes. Camm and Rose¹⁵ improved the correlation of the theory with low speed data and extended its range of validity to higher shock velocities by including the accurate boundary layer calculations of Kemp¹⁶ and correcting minor errors in the previous theories.

The equation governing the growth of the test time, as derived by Roshko¹³ and corrected by Camm and Rose,¹⁵ is:

$$\frac{1}{2} X = - \ln(1 - T^{1/2}) - T^{1/2} \quad (4.10)$$

where

$$X = 16 \left(\frac{\mu}{\rho a} \right)_0 \beta^2 \frac{Z_2 T_2}{T_1} \frac{a_1}{U_S} \frac{p_0}{p_1} \frac{x}{d^2} \frac{\eta - 1}{\eta} \quad (4.11)$$

$$T = 16 \left(\frac{\mu}{\rho a} \right)_0 \beta^2 \frac{Z_2 T_2}{T_1} \frac{a_1 \tau}{d^2} \frac{p_0}{p_1} \frac{(\eta - 1)^2}{\eta} \quad (4.12)$$

Here x is the shock travel distance, τ is the test time, d is the shock tube diameter, Z is the compressibility, a is the sound velocity, μ is the viscosity, η is the density ratio ρ_2/ρ_1 across the shock front, and β is a parameter proportional to the mass flux in the boundary layer evaluated by Kemp¹⁶ and Mirels.^{14,17} The subscript 0 refers to the standard reference state of the test gas (room temperature, 1 atm pressure), and the subscripts 1 and 2 refer to the initial and shocked state of the test gas.

Mirels¹⁴ corrected and extended the analysis of Roshko by accounting for variations in free stream conditions between the shock front and the contact surface. The corrected equation correlating shock travel distance with test time is

$$\frac{1}{2} X = - \ln(1 - T^{1/2}) - T^{1/2} - \frac{T}{2\eta} \quad (4.13)$$

Here

$$\eta = \rho_{e,0}/\rho_\infty \quad (4.14)$$

is the density ratio at the shock front. For strong shocks the Mirels correction term is small, and can be neglected.

4.2.2 One-Gas System

In a one-gas system the implosive driver, either jetting or jetless, directly drives the test gas with a massive piston. For an ideal piston there is no mechanism equivalent to the boundary layer leakage described above for reducing test time. Even for a nonideal piston the dominant effects limiting performance will probably not include boundary layer leakage, for there is no reason to suppose that the massive driving piston will flow over the boundary layer to provide a leakage path.

Boundary layer effects will, however, affect the uniformity of the test gas flow. Eventually the boundary layers will grow to sufficient size that they fill the entire shock tube, and turbulent pipe flow will result. In addition, because the cool boundary layer is much denser than the free stream, it acts as a condensing trap for the gas, and the remaining test gas will be cooled by expansion.

The size of the boundary layers can readily be estimated as a function of the test time τ . The viscous boundary layer thickness is given by

$$\delta = K \sqrt{\frac{\rho_2 \tau}{\mu_2}} \quad (4.15)$$

where K is a numerical factor depending on the definition of the edge of the boundary layer and the variation of the density, viscosity, and velocity through the boundary layer. Typical values for K range between 3 and 5; we shall choose $K = 5$ for an estimate.

The ratio between the thermal boundary layer and the viscous boundary layer is proportional to the square root of the Prandtl number; as an estimate we will take the proportionality factor to be unity.

A calculation of the boundary layer thicknesses for a test time of 10 μsec based on Hansen's estimates¹⁸ of the transport properties of high temperature air indicates that at a shock velocity of 15 km/sec and an initial pressure of 1 torr the viscous boundary layer thickness is 1.23 mm, and the thermal boundary layer thickness is 2.62 mm. Both boundary layer values are approximately proportional to the square root of the initial pressure and the square root of the test time.

4.3 Radiative Cooling

Obtaining a complete solution to the problem of radiative cooling and heat transfer is prohibitively difficult, but it is possible to solve an idealized problem that is closely related to the actual situation. Consider a shock wave propagating through the test gas at a constant velocity, so that the flow behind the shock front is steady and the flow properties depend only on the distance behind the shock front.

The radiative energy losses of the gas depend upon its temperature, absorptivity, and optical thickness. Only the case of an optically thin gas, however, is compatible with the assumption of one-dimensional flow; if the gas were optically thick the outer surface of the gas would cool more rapidly than the core, and nonuniform flow would result.

If we assume that the flow is one-dimensional and apply the conservation laws of mass, momentum, and energy to an element of test gas behind the shock, we obtain the equations:

$$\rho(U_S - u) = \rho_1 U_S \quad (4.16)$$

$$p - p_1 = \rho_1 u U_S \quad (4.17)$$

$$h + \frac{1}{2} (U_S - u)^2 = h_1 + \frac{1}{2} U_S^2 - Q(\xi) \quad (4.18)$$

Here ρ is the density, p is the pressure, h is the specific enthalpy, and u is the particle velocity of an element of gas a distance ξ behind the shock front. The subscript 1 refers, as usual, to the undisturbed gas in front of the shock, and U_S is the shock velocity.

$Q(\xi)$ is the integrated specific heat loss due to radiation as the element of gas moves from the shock front to a distance ξ behind the shock front:

$$Q(\xi) = \int_0^\xi q(\xi') d\xi' \quad (4.19)$$

Except for the heat loss term the equations are the usual Hugoniot equations holding across a shock, a result which follows from the assumed steady state nature of the flow.

Equations 4.17 and 4.18 may be rewritten using Eq. 4.16:

$$p - p_1 = \rho_1 U_S^2 (1 - \rho_1/\rho) \quad (4.20)$$

$$h - h_1 = \frac{1}{2} U_S^2 [1 - (\rho_1/\rho)^2] - Q(\xi) \quad (4.21)$$

For air shocked to velocities in the range 10 to 20 km/sec the density ratio across the shock, ρ_2/ρ_1 , is typically greater than 10. If the density ratio ρ/ρ_1 remains large when the gas is cooled by radiative losses, the pressure p is essentially constant and radiative losses are apparent only in the enthalpy of the gas.

As the radiative losses accumulate the enthalpy decreases at constant pressure; thus the process of radiative cooling moves the state point of the test gas in a straight line on an enthalpy-pressure chart. The thermodynamic state of the gas as it cools may be determined from this curve; the results of such a calculation are shown in Fig. 4.2.

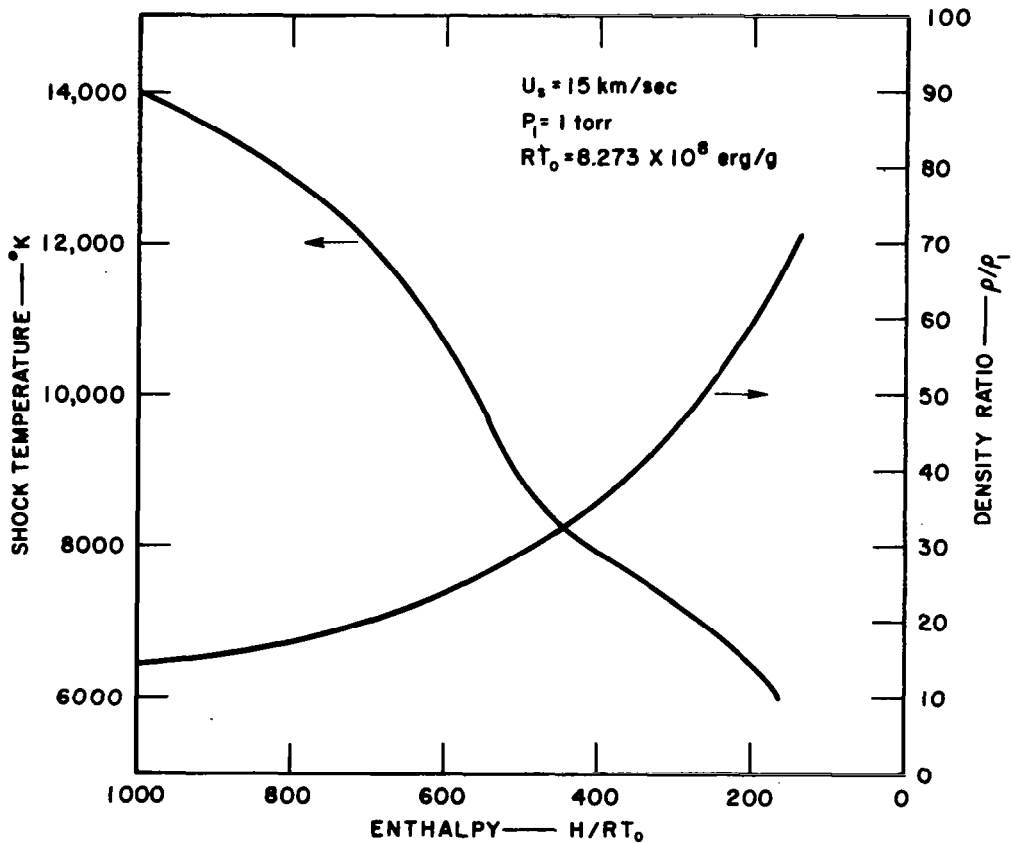


FIG. 4.2 RADIATIVE COOLING CURVE FOR AIR

The density ρ may be used to update the density ratio ρ/ρ_1 , which in turn may be used to refine the position of the cooling curve. For density ratios exceeding 10 the correction is negligible.

4.4 Conductivity Gage Analysis

4.4.1 DC Conductivity Gage

A dc conductivity gage was designed to determine the effective conductivity of the test gas by measuring its dc resistance. (Offered by the ionized test gas.) The gage consists essentially of two copper wires flush-mounted in a nonconducting material in the shock tube wall; the device operates by sending a constant current through the plasma and monitoring the voltage drop across the plasma as a function of time. The successful operation of the gage depends upon having the voltage drop due to the finite resistance of the plasma exceed the voltage drop across the Debye sheath. We assume in the following analysis that this condition holds, although no calculations have yet been performed to test the range of validity of this assumption.

An idealized form of the dc conductivity gage used in Shot 11,905 was analyzed mathematically to determine the resistance offered by the plasma as a function of conductivity. Since the wires contacting the plasma are much smaller than the shock tube diameter, so that most of the current flow would be directly across the tube, it seems reasonable to approximate the cylindrical cross-section of the shock tube by an infinite strip whose width is equal to the tube diameter. In addition the plasma is assumed to have a constant conductivity.

Let $d = 2a$ be the diameter of wire, $D = 2h$ the shock tube diameter and σ the conductivity of the plasma. The equations governing the vector current density \vec{J} and the electric potential ϕ are

$$\nabla^2 \phi = 0 \quad (4.22)$$

$$\vec{J} = -\sigma \nabla \phi \quad (4.23)$$

Equation 4.22 becomes, in a cylindrical coordinate system whose axis lies along the line connecting the wire centers,

$$\frac{1}{r} \frac{\partial}{\partial r} \left(r \frac{\partial \phi}{\partial r} \right) + \frac{\partial^2 \phi}{\partial z^2} = 0 \quad (4.24)$$

We assume the current density to be constant across the face of the wire; hence, for a given current I

$$\left. \frac{\partial \phi}{\partial Z} \right|_{\substack{Z=h \\ r \leq a}} = \frac{J}{\sigma} = \frac{4I}{\pi d^2 \sigma} = b \quad (4.25)$$

$$\left. \frac{\partial \phi}{\partial Z} \right|_{\substack{Z=-h \\ r \leq a}} = -\frac{J}{\sigma} = -b \quad (4.26)$$

and

$$\left. \frac{\partial \phi}{\partial Z} \right|_{\substack{Z=\pm h \\ r > a}} = 0 \quad (4.27)$$

We define the Bessel transform of ϕ by the equations

$$\bar{\phi}(\xi) = \int_0^{\infty} J_0(r\xi) \phi(r) r dr \quad (4.28)$$

$$\phi(r) = \int_0^{\infty} J_0(r\xi) \bar{\phi}(\xi) \xi d\xi \quad (4.29)$$

where J_0 is the Bessel function of the first kind. The transformed equation governing $\bar{\phi}$ is

$$\frac{d^2 \bar{\phi}}{dZ^2} - \xi^2 \bar{\phi} = 0 \quad (4.30)$$

which has the general solution

$$\bar{\phi} = A e^{\xi Z} + B e^{-\xi Z} \quad (4.31)$$

The transform of the boundary conditions described in Eqs. 4.25 through 4.27 is given by

$$\left. \frac{\partial \bar{\phi}}{\partial Z} \right|_{Z=h} = \int_0^a b J_0(r\xi) r dr = \frac{ab}{\xi} J_1(a\xi) \quad (4.32)$$

and similarly

$$\left. \frac{\partial \bar{\phi}}{\partial Z} \right|_{Z=-h} = -\frac{ab}{\xi} J_1(a\xi) \quad (4.33)$$

Hence the particular solution for the transformed potential is

$$\bar{\phi}(\xi Z) = \frac{ab}{\xi^2} J_1(a\xi) \frac{\sinh(\xi Z)}{\cosh(\xi h)} \quad (4.34)$$

The potential is obtained by using Eq. 4.29 to invert Eq. 4.34:

$$\phi(r, Z) = \int_0^\infty \frac{ab}{\xi} \frac{\sinh(\xi Z)}{\cosh(\xi h)} J_1(a\xi) J_0(r\xi) d\xi \quad (4.35)$$

In particular, the potential across the plasma is given by

$$V = 2\phi(0, h) = 2ab \int_0^\infty \frac{\tanh(\xi h)}{\xi} J_1(a\xi) d\xi \quad (4.36)$$

Hence the resistance of the plasma satisfies the equation

$$R = \frac{V}{I} = \frac{2h}{\pi a^2 \sigma} \cdot \frac{a}{h} \int_0^\infty \frac{\tanh(\xi h)}{\xi} J_1(a\xi) d\xi \quad (4.37)$$

This expression may be put into the form

$$R = R_0 f(d/D) \quad (4.38)$$

where

$$R_0 = \frac{4D}{\pi d^2 \sigma} \quad (4.39)$$

is the resistance of a wire with conductivity σ , diameter d , and length D . The function $f(d/D)$ is a correction factor to account for the spreading of the current through the plasma.

The integral can be put in the form

$$f(d/D) = \frac{d}{D} \int_0^\infty \frac{\tanh X}{X} J_1(Xd/D) dX \quad (4.40)$$

It may be evaluated in terms of K_1 , the modified Bessel function of the first kind:

$$f(d/D) = 1 - \frac{2d}{\pi D} \sum_{p=0}^{\infty} \frac{K_1 \left[\frac{\pi d}{D} \left(p + \frac{1}{2} \right) \right]}{\left(p + \frac{1}{2} \right)} \quad (4.41)$$

This function is plotted in Fig. 4.3.

The analysis has so far assumed a steady current flow through the plasma. In order to determine the response of the plasma to a suddenly applied voltage it is sufficient to determine the complex impedance as a function of frequency; the response to a step function input can then be calculated by the well-known methods of electric circuit theory. The equation governing the electric potential at a constant frequency ω is, neglecting wave propagation effects,

$$\nabla^2 \phi + k^2 \phi = 0 \quad (4.42)$$

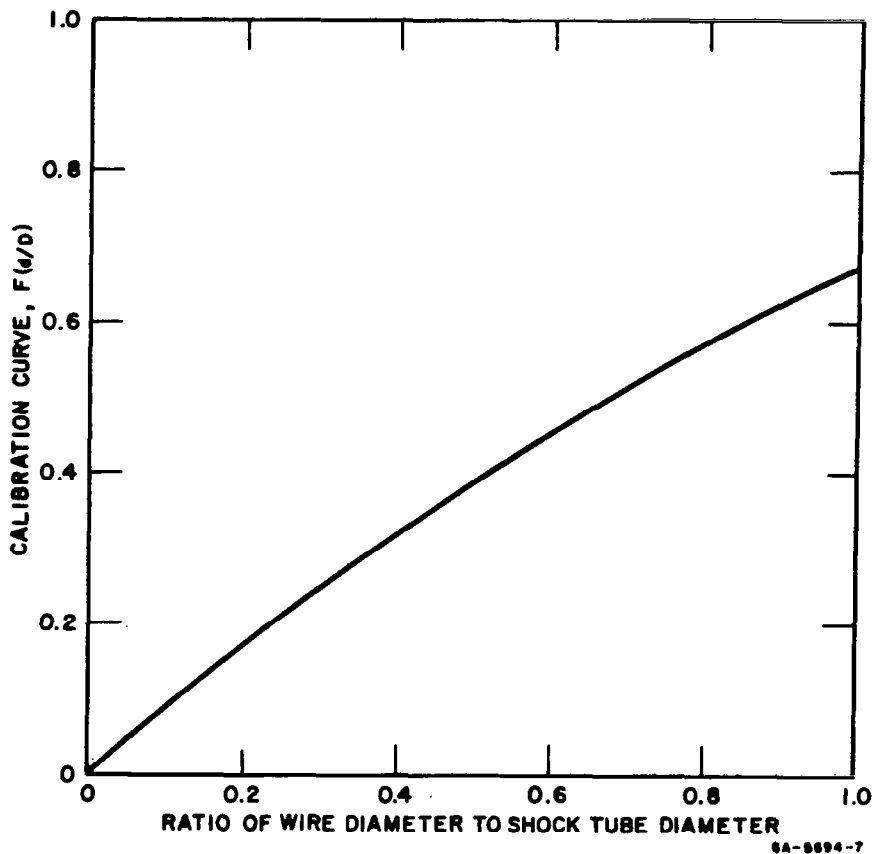


FIG. 4.3 DC CONDUCTIVITY GAGE INTEGRAL

where

$$k^2 = -j\omega\mu_0\sigma \quad (4.43)$$

Here j is the complex number $\sqrt{-1}$ and μ_0 is the magnetic permeability of space.

Applying the Bessel transform as in the dc case, we obtain the equation

$$\frac{d^2\phi}{dZ^2} - (\xi^2 - k^2)\bar{\phi} = 0 \quad (4.44)$$

This is exactly the same form as we found previously in Eq. 4.30, except that ξ^2 is replaced by $\xi^2 - k^2$. The equation, along with the boundary conditions, is solved in the same manner as was the dc equation, and we obtain

$$\bar{\phi} = \frac{I}{\pi a^2 \sigma} \cdot \frac{a}{\xi} J_1(a\xi) \frac{\sinh pZ}{p \cosh pZ} \quad (4.45)$$

where

$$p = \sqrt{\xi^2 - k^2} \quad (4.46)$$

The potential is obtained by inverting Eq. 4.45 using the Bessel inversion relation, Eq. 4.29:

$$\phi(r, Z) = \frac{I}{\pi a^2 \sigma} \cdot \int_0^\infty a \frac{\sinh pZ}{p \cosh pZ} J_1(a\xi) J_0(r\xi) d\xi \quad (4.47)$$

The complex impedance of the plasma as a function of the frequency ω is derived from the potential in the same manner as was the dc resistance in the previous case:

$$Z(\omega) = R_0 \frac{d}{D} \int_0^\infty J_1\left(X \frac{d}{D}\right) \frac{\tanh \sqrt{X^2 + j\omega\tau}}{\sqrt{X^2 + j\omega\tau}} dX \quad (4.48)$$

Here

$$X = \xi h,$$

and

$$\tau = \frac{\sigma \mu_0 D^2}{4} \quad (4.49)$$

is a characteristic relaxation time for the dc current flow to become established. When $\tau = 0$ or $\omega = 0$ the dc resistance of the plasma is recovered, as is easily seen by a comparison of Eq. 4.48 with Eq. 4.40. The integral cannot, however, be evaluated in terms of elementary functions for the ac case as it was for the dc case.

For typical experiments in air at shock velocities on the order of 15 km/sec, calculations indicate that τ is on the order of the test time. As a consequence, the dc resistance level across the plasma is never achieved, and determination of the plasma conductivity by analysis of the time variation of the resistance using Eq. 4.48 is required.

4.4.2 RF Gage

The determination of plasma conductivity by radio frequency (rf) measurements rather than dc measurements leads to significant practical and theoretical simplifications in addition to providing a great increase in time resolution. Air shocked to velocities on the order of 15 km/sec is a good conductor, and we are able to use the powerful techniques developed for microwave transmission lines in calculating gage response.*

The rf gage consists essentially of a folded coaxial cable, with the plasma acting as a shorting path between the inner and outer conductors (see Figs. 2.3 and 2.4). The attenuation of an rf signal passing through the cable is proportional to the shunt impedance offered by the plasma, which in turn is related to the plasma conductivity. Most of the current flow in the plasma is confined to a "skin depth" δ defined by

$$\delta = \sqrt{\frac{2}{\mu_0 \omega \sigma}} \quad (4.50)$$

where ω is the angular frequency of the signal, σ is the plasma conductivity, and μ_0 is the magnetic permeability of space. As a consequence of the small skin depth, typically on the order of a few tenths of a millimeter, the gage measures only the stagnation conductivity, and may be affected by boundary layers and the Debye shielding layer. For the present we assume these complications to be negligible, although no detailed calculations have been made to test the range of validity of the assumption.

* See for example, J. C. Slater, *Microwave Transmission*, Dover Publ., 1959, especially p. 138.

The shunt impedance Z may be related to the surface impedance Z_0 of the plasma by well-known techniques of microwave waveguide theory. The surface impedance of a good conductor is defined by the ratio of tangential electric field strength to tangential magnetic field strength:

$$Z_0 = \frac{E_t}{H_t} \quad (4.51)$$

and is given by

$$Z_0 = \sqrt{\frac{j\omega\mu}{\sigma}} \quad (4.52)$$

where j is the unit imaginary number.

To obtain the shunt impedance offered by the plasma the tangential magnetic field H_t is calculated for a plasma of infinite conductivity. It is then assumed that this tangential field does not change for a large but finite conductivity, and the tangential electric field is calculated from Eq. 4.51. The shunt impedance is then found by integrating the field strength to find the total potential drop, and dividing by the applied current. Thus we will have

$$Z = FZ_0 \quad (4.53)$$

where F is a geometrical factor depending upon the particular configuration of the rf gage.

In the case of the rf gage shown in Fig. 2.4 the calculations may be performed explicitly. The current I flows on the surface of the plasma over a dielectric annulus separating the inner conductor from the outer conductor. The surface current K as a function of radius r is easily seen to be

$$K = \frac{I}{2\pi r} \quad (4.54)$$

and the surface current is numerically equal to the tangential magnetic field strength. The tangential electric field is therefore given by

$$E_t = \frac{Z_0 I}{2\pi r} \quad (4.55)$$

and the potential drop across the plasma is

$$V = \int_a^b E_t dr = Z_0 I \frac{\ln b/a}{2\pi} \quad (4.56)$$

where b and a are the bounding radii of the dielectric annulus. The shunt impedance is given by the ratio of voltage drop to current:

$$Z = Z_0 \frac{\ln b/a}{2\pi} \quad (4.57)$$

5. CONCLUSIONS

5.1 Jetting Driver

The flow properties and driver characteristics of the jetting driver system were studied in detail during this project. It has been found that the jetting driver is most effective at initial air pressures less than 1 torr, and that at these low initial pressures the flow quality, duration, and purity are exceptional.

A theory was developed which appears to explain quantitatively the behavior of the jetting driver, including predictions of the jet mass, jet particle size, jet velocity, and effectiveness of the diffuse jet as a driving piston. This theory was developed late in the program, and insufficient data have been obtained to verify it completely. It does well, however, in correlating existing data.

One of the principal predictions of this theory is that the jetting driver operates best with a low pressure test gas. At high pressures the test gas leaks through the diffuse jet and the test time is reduced. At low initial pressures the Reynolds number of the jet particles decreases below unity, and the effective drag coefficient of the particles increases. Below 1 torr initial pressure the drag of the jet particles becomes so great that the diffuse jet acts like a solid piston, and no test gas is lost through the jet. This effect was in fact observed; the test time jumped dramatically when the pressure was decreased from 5 to 0.5 torr, and at the lower pressures the test time was found to be equal to the ideal maximum test time generated by a solid driving piston.

5.2 Jetless Driver

The jetless driver, driving a two-gas system in a manner resembling a conventional shock tube, was studied briefly. It was found that the measured test times corresponded very closely to the predictions of a boundary layer leakage theory. The real utility of the driver decreases as the initial test gas pressure is decreased; at initial pressures much below 1 torr the test time in a 37 mm shock tube approaches an unacceptably low maximum value, due to boundary layer leakage.

However, the jetless driver warrants further study when initial pressures greater than 1 torr are to be studied. The jetless driver has the advantage that high performance is obtained with a minimum amount of explosive; i.e., the fraction of explosive energy appearing in a useful form in the shock tube is greater for the jetless driver in a two-gas system than it is for a jetting driver directly driving the test gas.

5.3 Measurement Techniques

Much of this project has been concerned with developing and testing measurement techniques adequate to analyze the high energy gas flows generated by the implosive shock tube drivers. As a result, various techniques were developed for increasing the amount of information obtainable from high speed photographic instrumentation already installed at the SRI explosive test site. These techniques include several different methods for obtaining spectrally resolved absorptivity in the optical range, and a method for determining temperature by comparison with a calibrated high temperature source.

In addition an rf conductivity gage was developed for obtaining time- and space-resolved information on the scalar conductivity of the gas. This instrument was specifically designed for the high temperature, high density plasma expected at initial air pressures greater than 5 torr and shock velocities greater than 15 km/sec. In this regime the conductivity is greater than 150 mho/cm, and most measurement techniques developed for shock tubes operating at a lower conductivity level fail at these high levels. In addition the plasma is optically thick in a few centimeters at these energy levels, and optical techniques fail to provide useful information. Unfortunately, the conductivity gage was not fully studied during the project, since a decision was made to emphasize relatively low pressure test gases.

6. RECOMMENDATIONS FOR FUTURE WORK

The proven performance of the various implosive shock tube drivers, and especially of the jetting driver, opens up a number of interesting possibilities in studying the properties of high energy gases and radiatively coupled high energy flows. In particular, our knowledge of the basic physical properties of atmospheric gases at energies corresponding to planetary entry velocities can be greatly extended by a coordinated program using the implosive shock tube.

6.1 Laboratory Containment

It would be most useful in any experimental program using the implosive driver to be able to contain the explosive in a laboratory environment. Thus a major recommendation for future work is to study the feasibility of containing the blast from the implosive driver. This study should include an optimization of the amount of explosive used, a study of various types of containment techniques, and the design, construction, and test of a containment device.

6.2 Gas Properties

Paralleling the containment study should be an experimental program designed to measure as accurately as possible the radiative, transport, and thermodynamic properties of high energy gases. The implosive shock tube has been shown to be effective in generating high energy gas flows of exceptional uniformity, purity, and duration, and a large amount of experimental information can now be amassed for a regime where little data now exist. This work should not await the outcome of the containment study, as much valuable time would be lost unnecessarily; rather this should be a parallel program benefiting from any advances made during the containment study.

6.3. Simulation Studies

A further use of the implosive shock tube facility is to simulate conditions expected during planetary entry. Problems of radiatively

coupled flow, boundary layer phenomena, conductive and radiative heat transfer, and other questions of scientific and engineering interest can be closely simulated under controlled conditions. The wide range of velocity and pressure capabilities inherent in the implosive driver system allows a much closer simulation than is possible in most shock tube facilities, and the duration, uniformity, composition, and purity of the flow can be much more closely prescribed.

REFERENCES

1. G. R. Fowles, W. M. Isbell, and F. H. Shipman, "Feasibility Study of an Explosive Gun," Final Report, SRI Project GSU-4511, Contract NAS2-1361, July 5, 1964.
2. J. K. Crosby and S. P. Gill, "Feasibility Study of an Explosive Gun," Final Report No. 2, SRI Project GSU-4511, Contract NAS2-1361, May 1966.
3. D. B. Moore and J. K. Crosby, "Design and Application of a High-Speed Time-Resolving Spectrograph," *Proc. Fifth Internat. Cong. on High-Speed Photography*, J. S. Courtney-Pratt, ed. (Society of Motion Picture and Television Engineers, 1962).
4. J. Roth, "Measured Temperatures of Strong Shock Waves in Argon," *J. Appl. Phys.* **35**, 1429 (1964).
5. M. A. Pivovsky and M. R. Nagel, *Tables of Blackbody Radiation Functions*, MacMillan Company, New York, 1961.
6. Birkhoff, G., D. P. MacDougall, E. M. Pugh, and G. Taylor *J. Appl. Phys.* **19**, 563-582 (1948).
7. H. Schlichting, *Boundary Layer Theory*, McGraw-Hill Book Co., 1960.
8. Private communication, October 1966.
9. R. Kuthe, III, *Z. Flugwiss.* **13**, 136(1965); II, *Z. Flugwiss.* **12**, 407(1964); I, *Z. Flugwiss.* **12**, 374(1964).
10. F. W. Fenter and H. B. Gibbons, "The Thermodynamic Properties of High Temperature Air," Report No. RE-1R-14, Chance Vought Research Center, Dallas, Texas, 28 June 1961.
11. K. G. Sewell, F. W. Fenter, and H. B. Gibbons, "The Radiative Properties of Air in Thermodynamic Equilibrium," Report No. 0-71000/2R-26, Ling-Temco-Vought, Inc., July, 1962.
12. G. F. Anderson, *J. Aerospace Sci.* **26**, 184(1959).
13. A. Roshko, *Phys. Fluids* **3**, 835(1960).
14. H. Mirels, *Phys. Fluids* **6**, 1201(1963).
15. J. C. Camm and P. H. Rose, *Phys. Fluids* **6**, 663(1963).
16. N. H. Kemp (unpublished), quoted in Camm and Rose, op. cit.
17. H. Mirels, NASA TM D-291, 1961.
18. C. F. Hansen, "Approximations of the Thermodynamic and Transport Properties of High-Temperature Air," NACA TN-4150, 1958.